The relationship between CO emission and visual extinction traced by dust emission in the Magellanic Clouds

Cheoljong Lee,[1][*] Adam K. Leroy,[2,3] Scott Schnee,[3] Tony Wong,[4]
Alberto D. Bolatto,[5] Remy Indebetouw[1,3] and Monica Rubio[6]

[1]*Department of Astronomy, University of Virginia, Charlottesville, VA 22904, USA*
[2]*Department of Astronomy, The Ohio State University, 140 West 18th Avenue, Columbus, OH 43210, USA*
[3]*National Radio Astronomy Observatory, Charlottesville, VA 22903, USA*
[4]*Astronomy Department, University of Illinois, Urbana, IL 61801, USA*
[5]*Department of Astronomy, University of Maryland, College Park, MD 20742, USA*
[6]*Departamento de Astronomía, Universidad de Chile, Casilla 36-D, Santiago, Chile*

ABSTRACT

To test the theoretical understanding that finding bright CO emission depends primarily on dust shielding, we investigate the relationship between CO emission (I_{CO}) and the amount of dust (estimated from infrared emission and expressed as 'A_V') across the Large Magellanic Cloud (LMC), the Small Magellanic Cloud, and the Milky Way. We show that at our common resolution of 10 pc scales, I_{CO} given a fixed line of sight A_V is similar across all three systems despite the difference in metallicity. We find some evidence for a secondary dependence of I_{CO} on radiation field; in the LMC, I_{CO} at a given A_V is smaller in regions of high T_{dust}, perhaps because of an increased photodissociating radiation field. We suggest a simple but useful picture in which the CO-to-H_2 conversion factor (X_{CO}) depends on two separable factors: (1) the distribution of gas column densities, which maps to an extinction distribution via a dust-to-gas ratio; and (2) the dependence of I_{CO} on A_V. Assuming that the probability distribution function (PDF) of local Milky Way clouds is universal, this approach predicts a dependence of X_{CO} on Z between Z^{-1} and Z^{-2} above about a third solar metallicity. Below this metallicity, CO emerges from only the high column density parts of the cloud and so depends very sensitively on the adopted PDF and the H_2/H I prescription. The PDF of low-metallicity clouds is thus of considerable interest and the uncertainty associated with even an ideal prescription for X_{CO} at very low metallicity will be large.

Key words: ISM: clouds – ISM: molecules – galaxies: ISM – Magellanic Clouds.

1 INTRODUCTION

As the immediate reservoir for star formation, the molecular interstellar medium (ISM) plays a key role in the evolution of galaxies. Unfortunately, the majority of cold molecular hydrogen (H_2) in typical clouds is invisible in emission due to the fact that the H_2 molecule has low mass and therefore requires high temperatures (the lowest level corresponds to $E/k \approx 510$ K) to excite its rotational transitions (Kennicutt & Evans 2012). As a result, astronomers employ a suite of more observationally accessible tracers of H_2 to study molecular clouds. Low J rotational transitions of CO represent the most accessible and commonly used such tracers, especially in external galaxies. The abundance, pervasiveness, and brightness of

CO make it a useful tracer, but it is not perfectly co-extant with H_2 and the relationship between CO emission and H_2 column density (so-called 'CO-to-H_2 conversion factor', X_{CO}) is both expected and observed to vary systematically as local conditions change (see the review by Bolatto, Wolfire & Leroy 2013). Consequently, it is important to understand the physical origins of CO emission and their implications for the use of CO emission to trace H_2.

Coarsely, variations in X_{CO} are twofold. The regions in a molecular cloud where CO and H_2 exist are not perfectly matched, with a layer of CO-poor H_2 extending beyond the region at which the dominant form of carbon changes from CO to C II (e.g. Maloney & Black 1988; van Dishoeck & Black 1988). Theoretically, the amount of dust shielding (A_V) between the CO–C II transition layer and the H_2–H I transition layer is estimated to be almost constant (Wolfire, Hollenbach & McKee 2010). This is also seen in photodissociation region (PDR) calculations (Bell et al. 2006) and numerical

[*] E-mail: cl5ju@virginia.edu

simulations (Glover & Mac Low 2011; Shetty et al. 2011), where I_{CO} exhibits a clear dependence on A_V. In a low-metallicity cloud the dust-to-gas ratio is also low, so that achieving some fixed A_V requires a much larger column of gas than at high metallicity. Therefore this intermediate region of H_2 without much associated CO becomes very large in terms of total gas content. As a result, one expects to find less CO emission per unit H_2 in clouds with a low metallicity. This gives rise to a dust-to-gas ratio, and thus metallicity, dependent term in X_{CO}. Meanwhile, within region where CO is abundant, the line is usually optically thick. This leads the ratio of CO emission to gas mass in this region to depend on density, temperature, and potentially other dynamical factors (e.g. see Maloney & Black 1988; Downes & Solomon 1998; Narayanan et al. 2012).

In this paper, we focus on the first part of the problem, the metallicity-dependent term in X_{CO}. We focus on the relationship between dust abundance along the line of sight and the brightness of CO emission (the 'I_{CO}–A_V' relation) as a way to explore the physics of CO emission and its utility as a tracer of H_2. Because theoretical models highlight the key role of dust shielding in setting the extent of bright CO emission, our hypothesis is that across diverse environments we will often find about the same amount of CO emission per unit dust shielding.

Highly resolved (sub-pc) observations of individual nearby clouds have explored the I_{CO}–A_V relationship in detail (Lombardi, Alves & Lada 2006; Pineda, Caselli & Goodman 2008; Pineda et al. 2010). These provide strong observational support for the crucial role of A_V in determining the amount CO emission. These high-resolution studies also reveal distinct regimes in the relationship, such as an extinction threshold below which CO emission is faint or absent, a linear rise of I_{CO} at intermediate extinctions, and evidence for saturation at high extinctions. The relationship has not been explored as much outside the Milky Way because of the coarse physical resolution in most CO and dust maps of other galaxies. However, studying a molecular complex in the Small Magellanic Cloud (SMC) at ≈ 10 pc resolution, Leroy et al. (2009) did observe an I_{CO}–A_V relationship that resembled that for a Milky Way cloud (their fig. 7).

Several new data sets make it possible to revisit the relationship between dust and CO emission in the Magellanic Clouds over a much wider area. The Magellanic Mopra Assessment (MAGMA; Wong et al. 2011) obtained high spatial resolution (~ 10 pc) CO $J = 1 \rightarrow 0$ data across most areas of bright CO emission in the Large Magellanic Cloud (LMC). A new Atacama Pathfinder Experiment (APEX) survey of the south-west part of the SMC (Rubio et al., in preparation) provides similar coverage in that galaxy; we also use previously published CO $J = 2 \rightarrow 1$ and $J = 1 \rightarrow 0$ maps of the N83 complex in the SMC Wing (Bolatto et al. 2003). Key projects by *Spitzer* (Surveying the Agents of a Galaxy's Evolution, SAGE Meixner et al. 2006) and *Herschel* (Herschel Inventory of the Agents of Galaxy Evolution, HERITAGE; Meixner et al. 2010, 2013) allow us to model infrared (IR) emission to estimate the line of sight extinction. This provides a handle on the total extinction (or dust column) through a part of the galaxy, which offers an imperfect but observationally accessible analogue to the physically crucial shielding of material from the interstellar radiation field (ISRF). Clearly, the relation between the total dust column (expressed by 'A_V') and the degree of shielding towards an average CO molecule depends on geometry, but even in simulations A_V and real shielding appear closely related (e.g. see Glover & Mac Low 2011). Thus, we now have a handle on CO emission and dust column at ≈ 10 pc resolution over a matched area for the two nearest (~ 50 kpc for the LMC and 60 kpc for the SMC; Keller & Wood 2006) star-forming

low-metallicity galaxies ($\sim 1/2$ $Z_\odot$ for the LMC and 1/5 $Z_\odot$ for the SMC; Westerlund 1997).

Combining these data on the Magellanic Clouds with Milky Way data from *Planck* and the Dame, Hartmann & Thaddeus (2001) CO survey, we are able to ask how the CO intensity, I_{CO}, at a given line of sight extinction, A_V, compares between the Milky Way, the LMC, and the SMC. Do successive steps of a factor of ≈ 2 in metallicity have a visible impact on I_{CO} at a given A_V or is the amount of dust shielding alone the key parameter? We also search for secondary factors affecting I_{CO} at fixed A_V, with the most obvious candidate being the ISRF, which is directly traced by the dust temperature. This might be expected to influence the amount of CO emission at a given line of sight extinction in two ways: first lowering the amount of CO emission by raising the number of dissociating photons and so requiring more dust shielding for the transition from C II to CO. Second, perhaps increasing the temperature of the CO and so increasing I_{CO}.

In the second part of the paper, we explore the implications of a universal I_{CO}–A_V relation for the CO-to-H_2 conversion factor, X_{CO}. If I_{CO} is largely set once A_V is known, then the distribution of A_V becomes the key factor to predict CO emission. This, in turn, depends on the probability distribution function (PDF) of gas column densities and the gas-to-dust ratio. The PDF of individual clouds in the Milky Way has been the study of significant quantitative study in recent years (see Kainulainen et al. 2009, and following). We combine these results with our estimates of the I_{CO}–A_V relation to make an empirically driven estimate of how X_{CO} depends on metallicity.

2 DATA AND MODELLING

We aim to compare CO emission to the line of sight extinction, estimated from IR emission, on the scale of individual clouds (~ 10 pc). To do so, we assemble matched-resolution CO (Section 2.1) and IR emission maps (Section 2.2) for the LMC, SMC, and Milky Way. We use the IR data to estimate the line of sight extinction (Section 2.3) and so estimate I_{CO} as a function of A_V.

2.1 CO data

2.1.1 LMC

We use the second release of the MAGMA (Wong et al. 2011) survey[1] to generate an integrated intensity ('moment 0') map of CO emission from the LMC. MAGMA used the 22-m Mopra telescope to observe the CO $J = 1 \rightarrow 0$ transition towards molecular clouds identified from NANTEN surveys (Fukui et al. 1999, 2008). MAGMA has an angular resolution of 45 arcsec, ≈ 10 pc at the distance of the LMC. The mean rms brightness temperature of the MAGMA cube in a single channel (0.5 km s^{-1}) is 0.3 K (Wong et al. 2011). We generate the integrated intensity map by directly integrating the cube along the whole velocity axis ($180 \leq V_{LSR} \leq 320$ km s^{-1}).

For both theoretical and practical reasons, our analysis will treat A_V as the independent variable. A_V is expected to set the amount of CO emission and IR emission is detected at higher signal-to-noise ratio (S/N) than CO throughout the Magellanic Clouds. Reflecting this, we work with integrated intensity derived from a broad velocity window that will include any CO emission from the LMC. This

---

[1] http://mmwave.astro.illinois.edu/magma/DR2b/

directly integrated intensity map is not clipped or masked and so includes both positive and negative values. The advantage of this approach is that by averaging together many spectra at the same A_V we can recover a mean I_{CO} that is too faint to be detected in an individual line of sight. A corollary of this approach is that we are sensitive to small zero-point offsets in the data. Therefore, we subtract a constant baseline from the MAGMA data cube pixel-by-pixel, with the value determined from the median intensity of each line of sight from the signal-free edge channels at the edge of the data cube. The median offset in the zero level is very small, corresponding to only ∼1.2 mK and only important because some of our analysis focuses on faint regions. In Appendix A1 we show the quantitative effects of varying our baseline treatment, which is very minor compared to other uncertainties in the analysis.

2.1.2 SMC

For the SMC, we use a new APEX survey of CO $J = 2 \rightarrow 1$ emission from the south-west region of the SMC data (PI: Rubio; Rubio et al., in preparation). The angular resolution of the data is ∼28 arcsec, corresponding to ≈8 pc at the distance of the SMC, and rms noise is 0.3 K in each 0.1 km s^{-1} channel. These data target the south-west part of the SMC bar, which contains most of the ongoing star formation and molecular gas in the SMC. We also use Swedish-ESO Submillimetre Telescope (SEST) observation of CO $J = 2 \rightarrow 1$ and $J = 1 \rightarrow 0$ emission from the star-forming complex N83 located in the wing of the SMC (Bolatto et al. 2003). These data have angular resolution of 38 arcsec ($J = 2 \rightarrow 1$) and 55 arcsec ($J = 1 \rightarrow 0$) and rms noise 0.1 K in a 0.25 km s^{-1} channel for both lines.

As in the LMC, we directly integrate these data along the velocity axis to generate integrated CO intensity maps of the south-west SMC, picking a velocity range that covers the whole region and carrying out no other 'masking'. The velocity ranges of integration are $80 \leq V_{LSR} \leq 160$ km s^{-1} for the south-west SMC and $140 \leq V_{LSR} \leq 187$ km s^{-1} for N83.

2.2 Infrared maps

We use observations of IR dust emission in the LMC and the SMC at four different wavelengths from the HERITAGE survey: 100 and 160 μm images from the Photoconductor Array Camera and Spectrometer (PACS) instrument, and 250 and 350 μm images from the Spectral and Photometric Imaging Receiver (SPIRE) instrument. The angular resolutions of these maps are 7.7 arcsec (100 μm), 12 arcsec (160 μm), 18 arcsec (250 μm), and 25 arcsec (350 μm), so that the CO data set the limiting resolution for our analysis.

Before proceeding to our analysis, we convolved the IR maps in the LMC to the 45 arcsec resolution of the MAGMA CO map. This is done by first using the convolution kernels of Aniano et al. (2011) to convolve HERITAGE maps to a common point spread function (PSF; we used the *Spitzer* 160 μm for comparison with *Spitzer* work) and then degrade them together to the 45 arcsec resolution of the MAGMA CO data. We place all LMC data on the same astrometric grid, which has pixel spacing of 15.6 arcsec.

We take a similar approach to match the resolutions and grids of IR maps in the SMC. Here we match the *Herschel* data to the 28 arcsec resolution of the CO $J = 2 \rightarrow 1$ transition in the south-west region of the SMC, to the 38 arcsec resolution for the CO $J = 2 \rightarrow 1$ transition in N83, and to the 55 arcsec for the $J = 1 \rightarrow 0$ transition in N83. Again all data are placed on a shared astrometric grid.

The 1σ noises of the LMC IR maps at our working resolution (45 arcsec) are $\sigma_{100} \sim 2.3$ MJy sr^{-1}, $\sigma_{160} \sim 2.4$ MJy sr^{-1}, $\sigma_{250} \sim 0.88$ MJy sr^{-1}, and $\sigma_{350} \sim 0.48$ MJy sr^{-1}. In our analysis we consider only regions with intensity at least three times these values in each band. We refer to the 'LMC field' as the region that satisfies this S/N ratio cut in the IR maps, while the 'MAGMA field' is defined as the region in the LMC field where the MAGMA survey mapped in CO. The MAGMA field is a subset of the LMC field.

The noises in the SMC IR maps are similar but vary with resolution. We estimate the noise at each working resolution and again mask regions below 3σ in the IR maps. As above, the 'SMC field' is the region where IR maps have values greater than 3σ at high resolution, while the 'APEX field' and 'SEST field' are the regions within the SMC field where APEX telescope and SEST telescope mapped CO emission.

Note that a first-order (linear) baseline has been already subtracted from the IR maps in the HERITAGE release to remove emission not associated with the Magellanic Clouds themselves from the maps (Meixner et al. 2013). We do not apply any further correction to account for Milky Way foreground dust emission, though we do model a level of uncertainty in this subtraction by including a zero-point uncertainty in our Monte Carlo analysis (Section 2.3.3).

2.3 Estimation of the 'A_V' map

We use the *Herschel* IR emission maps to estimate 'A_V' along each line of sight through the LMC and the SMC. Here A_V refers to visual extinction, measured in magnitudes estimated from the optical depth at 160 μm, τ_{160}. We calculate this by fitting a modified blackbody to the measured IR intensities (Section 2.3.1) and then converting the dust optical depth to visual extinction following an empirical scaling derived from the Milky Way (Section 2.3.2). Because the dust emission is optically thin, 'A_V' measured in this way will probe material along the whole line of sight and averaged over the substantial beam of the *Herschel* data. This is similar to extinction mapping for nearby molecular clouds, which uses sources behind the cloud to create a large-scale map. It differs from true extinction mapping using internal sources in the Magellanic Clouds (e.g. stars), which will measure the extinction only part of the way through the galaxy.

2.3.1 Modified blackbody fit

We assume that the dust along a line of sight can be described as an optically thin ($\tau \ll 1$) grey body at an equilibrium temperature T_{dust}, and wavelength dependence of dust optical depth is a power law with spectral index β, i.e. $\tau_\lambda \propto \lambda^{-\beta}$ (e.g. Draine & Lee 1984). In this case the optical depth at 160 μm (τ_{160}) is given by

$$\tau_{160} = \frac{I_{160}}{B_\nu(T_{dust}, 160\,\mu m)}, \tag{1}$$

where I_{160} is the observed 160 μm intensity and $B_\nu(T_{dust}, \lambda)$ is the intensity of a blackbody of temperature T_{dust} at wavelength λ.

Because we have dust emission intensities measured at four different wavelengths, in principle we can fit for the three unknowns β, τ_{160}, and T_{dust}. Instead we adopt a fixed $\beta = 1.5$ as our fiducial value and fit for two unknowns τ_{160} and T_{dust} by minimizing the χ^2 from observed IR intensities and the model IR intensities,

taking the colour correction[2] for each filter into account. We fix β in order to minimize the uncertainties on the T_{dust} (and thus τ_{160}) arising from the fact that β and T_{dust} are somewhat degenerate in χ^2 space (Dupac et al. 2003). The adopted β above is a reasonable description of the integrated spectral energy distribution (SED) of the LMC (Bernard et al. 2008; Gordon et al. 2010; Planck Collaboration XVII 2011) and the SMC (Stanimirovic et al. 2000; Aguirre et al. 2003; Leroy et al. 2007), and is intermediate in the range of plausible astrophysical values, $1.0 < \beta < 2.0$ (Draine & Lee 1984; Schlegel, Finkbeiner & Davis 1998).

2.3.2 Conversion to A$_V$

Our modified blackbody fit yields the optical depth at 160 μm, τ_{160}. We wish to phrase our analysis in terms of the line of sight *V*-band extinction, A_V, which is the conventional unit expressing shielding in discussion of PDRs. We translate τ_{160} to A_V via

$$A_V \sim 2200\tau_{160}. \qquad (2)$$

We arrive at this conversion in several ways and take the differences among the estimates to indicate the uncertainty in the conversion. First, following Leroy et al. (2009), we infer $\tau_{160} = 2.44 \times 10^{-25}$ $N(\text{H\,\textsc{i}})$ from Diffuse Infrared Background Experiment (DIRBE)/Far-Infrared Absolute Spectrophotometer (FIRAS) observations of the Galactic diffuse H\,\textsc{i} (Boulanger et al. 1996). Then, we adopt the relation between colour excess of solar neighbourhood stars and H\,\textsc{i} column density from Lyα absorption, $E(B-V) = N(\text{H})/5.8\times 10^{21}$ cm^{-2} (Bohlin, Savage & Drake 1978). Taking a Galactic $R_V = 3.1$, we estimate $A_V \sim 2190\tau_{160}$.

We compare this number to the Schlegel et al. (1998) conversion used to estimate Galactic extinction maps from *IRAS* data. After correction to a fiducial dust temperature, they find $E(B-V) = (0.016 \pm 0.004) I_{100}^T$, where I_{100}^T is the 100 μm intensity after correction to a fixed 18.2 K temperature, and $E(B-V)$ is reddening measurement of background elliptical galaxies. Again taking $R_V = 3.1$ and assuming $\beta = 2$ for Galactic dust,[3] the Schlegel et al. (1998) conversion corresponds to $A_V \sim 1939\tau_{160}$. More recently, Planck Collaboration XI (2014) find systematically higher dust temperature and thus lower dust optical depth at high Galactic latitude using *IRAS* and *Planck* data. This is mainly due to the observed dust emission SED being flatter ($\beta \approx 1.59$) than previous studies. This leads to a higher $E(B-V)$ per dust optical depth (τ), where the former is from Sloan Digital Sky Survey (SDSS) quasars. Adopting $R_V = 3.1$ and β from their study, the conversion is $A_V \sim 3246\tau_{160}$.

This conversion can also be related directly to the mass absorption coefficient of dust, κ, following Hildebrand (1983). We consider $\tau_{160} = \Sigma_{dust}\kappa_{160}$. In the Milky Way, Hildebrand (1983) suggests $\kappa_{250} \approx 10$ cm^2 g^{-1}, which we convert to 160 μm assuming $\beta = 2$. Then taking the relation between $E(B-V)$ and $N(\text{H})$ above and assuming a dust-to-gas mass ratio of $\sim$1-to-150 (Draine et al. 2007) and $R_V = 3.1$, we arrive at $A_V \sim 1443\tau_{160}$.

To synthesize, calculations based on Milky Way studies suggest $A_V = (1400$–$3200)\tau_{160}$, with the mean conversion corresponding

to $A_V \approx 2200\tau_{160}$, which is the conversion we use in this paper. The fractional uncertainty above approximately matches that of Schlegel et al. (1998), and we fold it in to our Monte Carlo analysis to account for the uncertainties in the conversion from τ_{160} to A_V (see Section 2.3.3).

There are several direct measurements of $E(B-V)$ and A_V in the LMC. Our τ_{160} map has complete coverage and high S/N compared to these maps, so they do not offer a viable replacement, but we use them to check our adopted conversion from τ_{160} to A_V (equation 2). We compare to three data sets: the A_V map estimated by Zaritsky et al. (2004), which is based on photometry of individual 'hot' stars; the compilation of spectroscopic measurements from Welty et al. (2012); and the A_V map inferred from the near-IR (NIR) colour excess method by Dobashi et al. (2008) using Two Micron All Sky Survey (2MASS) data. In all cases, we restrict the comparison to regions that have $A_V > 0.5$ mag in our far-IR (FIR)-based A_V map. Zaritsky et al. (2004) and Welty et al. (2012) report extinction to LMC sources that we expect, on average, to lie halfway through the galaxy. To compare to our map, which samples the whole column, we multiply those data by a factor of 2 to account for the difference in geometry. The Dobashi et al. (2008) map already accounts for the distribution of stars along the line of sight and attempts to report an integrated extinction. Fig. 1 shows the resulting comparison as a histogram of the ratio between our map and these other estimates.
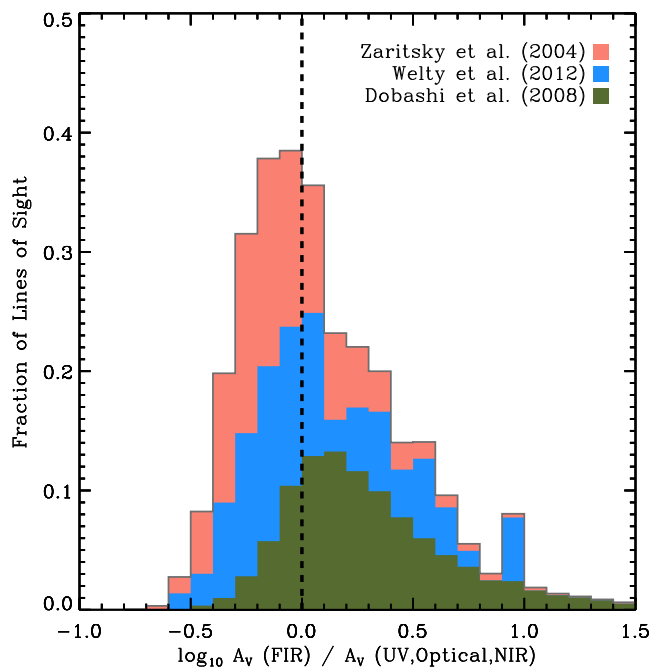

Figure 1. Comparison of our FIR-based A_V estimate to A_V inferred from stellar photometry (Zaritsky et al. 2004), UV spectroscopy (Welty, Xue & Wong 2012), and NIR colour excess (Dobashi et al. 2008) in the LMC. The log ratio of the former to the latter ($\log_{10} A_V^{\text{FIR}}/A_V^{\text{UV,Opt,NIR}}$) is shown on the *x*-axis, and the fraction of lines of sight is shown on the *y*-axis. The histogram for Zaritsky et al. (2004) is shown on top of the Welty et al. (2012) histogram, which is on top of the Dobashi et al. (2008) histogram. We expect the Zaritsky et al. (2004) and Welty et al. (2012) A_V estimates to sample only about half of the LMC, on average, and so scale these estimates by a factor of 2 in the plot. The dotted line indicates a ratio of unity. This lies close to the centre of the sum of three histograms, indicating an overall agreement between our approach to estimate A_V from the FIR and direct measurements, though there is substantial scatter and systematic effects remain. (A colour version of this figure is available in the online journal.)

---

[2] See http://herschel.esac.esa.int/twiki/pub/Public/PacsCalibrationWeb/cc_report_v1.pdf for PACS colour correction and http://herschel.esac.esa.int/hcss-doc-11.0/load/spire_drg/html/ch05s07.html for SPIRE colour correction.

[3] In comparing our τ_{160}–A_V conversion to other works, we use β assumed in each study rather than our fiducial $\beta = 1.5$.

Our FIR-based map yields lower A_V, on average than stellar photometry or UV spectroscopy, after the factor of 2 scaling of the optical and UV estimates. We find median $A_V^{\mathrm{FIR}}/A_V^{\mathrm{Opt,NIR}} \approx 0.75$ for the Zaritsky et al. (2004) data and median $A_V^{\mathrm{FIR}}/A_V^{\mathrm{UV}} \approx 0.95$ comparing to the Welty et al. (2012) data. In both cases we observe significant scatter, ≈ 0.24 dex in the Zaritsky et al. (2004) case and ≈ 0.33 dex comparing to Welty et al. (2012). Much of the large scatter likely reflects the internal geometry of the LMC or, for Welty et al. (2012), the difference between our large beam and the single pencil beam sampled by their spectroscopy. On the other hand, the FIR-based A_V yields somewhat higher A_V than the NIR colour excess method. We find median $A_V^{\mathrm{FIR}}/A_V^{\mathrm{NIR}} \approx 1.6$, again with large scatter (0.33 dex). Altogether, the sum of three histograms is approximately centred at a ratio of unity (dotted line). Given the stark difference in approaches to estimate the extinction we view these comparisons as reasonable confirmation of our adopted A_V/τ_{160} and overall approach. We take them to confirm the ≈ 50 per cent systematic uncertainty in A_V/τ_{160} discussed above.

2.3.3 Estimating the uncertainties in τ_{160} and A_V

We are primarily interested in the average relation between A_V and I_{CO} in the Magellanic Clouds. To estimate the uncertainties involved in the A_V portion of this relation, we adopt a Monte Carlo approach. We use the LMC data as a basis to repeatedly recalculate our A_V map while varying our assumptions across their plausible range. Each time that we do so, we add a new realization of the statistical noise to the data. We begin with the true LMC maps. We then add Gaussian noise with magnitude matched to the measured statistical noise to each map. For each new map, we also vary the zero-point of the maps within the estimated uncertainty. Doing so, we generate 100 new maps that could be realistic observations if the observed LMC maps were indeed the true intensity on the sky. For each set of these noise-added maps, we generated 10 sets of T_{dust} and τ_{160} maps following the χ^2 minimization described in Section 2.3.1. For these maps instead of fixing β at 1.5, we fixed it randomly at a value within its plausible ranges, $1 < \beta < 2$. In the end, we have 1000 maps with a spread that captures our true uncertainty regarding the derivation of A_V, except the conversion from τ_{160} to A_V. We take this into account by randomly taking a plausible conversion from τ_{160} to A_V as determined in Section 2.3.2, $A_V/\tau_{160} = (1400\text{–}3200)$, resulting in 1000 A_V maps.

Based on these calculations, we calculate the 1σ fractional scaling uncertainty associated with T_{dust}, 10 per cent, and with A_V, 45 per cent. That is, the whole map is uncertain by this amount due to zero-point uncertainties and methodological decisions. This is a correlated error that will adjust the entire map. The exercise and the scatter would be almost the same for the SMC, so we take these errors as representative of both galaxies. In the following figures discussing I_{CO}–A_V relationships, we show this error estimate for A_V as the horizontal error bars in the bottom right-hand corners to represent the typical uncertainty in A_V.

2.3.4 Limitations of our approach

Our approach to estimate 'A_V' has limitations, both due to our adopted approach and the use of IR emission to trace dust. We model a single population of isothermal dust along each line of sight. In reality, a mixture of temperatures and grain properties are present along each line of sight. This leads to biases in the total dust column determination (e.g. see Schnee et al. 2005, 2007,

2008; Schnee, Bethell & Goodman 2006 for detailed discussion) and could potentially affecting A_V/τ_{160}. These biases are somewhat alleviated by the inclusion of the long wavelength *Herschel* data and the very high (by extragalactic standards) spatial resolution of *Herschel* at the LMC. Ultimately, they correspond to fundamental degeneracies in modelling the IR SED to derive a dust column. Resolution clearly represents another limitation; while 10 pc resolution is the best achievable outside the Milky Way, this is still very coarse compared to substructure observed in Milky Way clouds, so that measured 'A_V' corresponds to something more like an average extinction across a Milky Way cloud than a value within a cloud. Finally, the properties of the dust are expected to change at some level, so that A_V/τ_{160} is not only uncertain in the absolute sense but may vary from location to location, e.g. due to grain coagulation or the growth of mantles. This may produce some of the scatter in our comparison to direct extinction measures above. Future observations with Atacama Large Millimeter/submillimeter Array (ALMA), *Hubble Space Telescope* (*HST*), and ground-based photometry all offer the potential to improve this work substantially. In the meantime, we present a first-order comparison using the best publicly available data.

2.3.5 Comparison between Herschel and Spitzer results

Before longer wavelength *Herschel* data were available, we modelled IR emission in the LMC using *Spitzer* 70 and 160 µm maps from SAGE survey (Meixner et al. 2006). We used comparisons to coarser resolution data at 100 µm to help us account for the out-of-equilibrium emission from very small grains (VSGs) contributing to the IR emission at 70 µm, finding about 50 per cent of the emission to represent contamination but otherwise the approach was very similar to our main results here. Table 1 compares the median and standard deviation of T_{dust} and A_V in the MAGMA field between *Spitzer* and *Herschel*. On average, T_{dust} from *Spitzer* is ~ 11 per cent lower than our best-fitting value from *Herschel*, while we find a ~ 32 per cent higher A_V using *Spitzer* than we do with *Herschel*. The point-by-point correlation between the maps is good, with a Pearson coefficient of $p = 0.76$ and 0.9 from comparing T_{dust} and A_V between maps derived from the two telescopes. Consequently, the qualitative results of this paper would remain unchanged if we use dust properties derived from either telescope. For our purposes, the main change would be that the slope in the I_{CO}–A_V relation is somewhat lower if we use only *Spitzer* data.

As a sanity check, we also compare to Skibba et al. (2012), who used the HERITAGE data to derive dust temperature and dust mass in the Magellanic Clouds. They fit a modified blackbody with $\beta = 1.5$ at $\lambda \leq 300$ µm and a different β that is allowed to vary to best describe the observation at 350 and 500 µm. We relate our estimate of τ_{160} to their dust mass estimate using their adopted mass absorption coefficient, $\kappa_{160} \approx 13.75 \, \mathrm{cm^2 \, g^{-1}}$. Using this κ_{160}, $D_{\mathrm{LMC}} = 50$ kpc, and $D_{\mathrm{SMC}} = 60$ kpc, our LMC τ_{160} map contains $\sim 1.0 \times 10^6 \, \mathrm{M_\odot}$, within 10 per cent of the $\sim 1.1 \times 10^6 \, \mathrm{M_\odot}$ found by Skibba et al. (2012) and also similar to the $\approx 1.2 \times 10^6 \, \mathrm{M_\odot}$ found

Table 1. Comparison of T_{dust} and A_V in MAGMA field.

	$\langle A_V \rangle$ (mag)	$\sigma(A_V)$ (mag)	$\langle T_{\mathrm{dust}} \rangle$ (K)	$\sigma(T_{\mathrm{dust}})$ (K)
Spitzer	0.911	0.940	21.8	1.84
Herschel	0.637	0.627	24.1	2.82

using *Spitzer* data by Bernard et al. (2008). In the SMC field, we find ~0.9×10^5 M$_\odot$ in our bright lines of sight, again just slightly below the ~1.1×10^5 M$_\odot$ from Skibba et al. (2012). Considering potential issues with aperture matching and subtleties of fitting, our maps appear very consistent with previous works.

2.4 Coverage and *A*$_V$ distribution in the Magellanic Clouds

As a targeted follow-up survey, MAGMA does not cleanly sample the distribution of *A*$_V$ in the LMC. Instead, MAGMA preferentially samples high extinction lines of sight. Likewise, a similar bias in *A*$_V$ is expected for the APEX and SEST fields in the SMC. Fig. 2

shows the maps of dust temperature ($T_{\rm dust}$) and dust optical depth (τ_{160}) scaled to visual extinction (A_V) in the LMC (upper panels) and SMC (lower panels) fields. The solid black contours show the regions covered by CO maps in each galaxy, the MAGMA field for the LMC and the APEX and SEST fields for the SMC. The upper right-hand panel clearly shows that dust shielding (estimated from τ_{160}) in the MAGMA field is enhanced compared to other regions in the LMC. This also appears to be the case for the APEX and SEST fields in the SMC. Considering the fact that the MAGMA field harbours the brightest molecular clouds identified by previous CO surveys in the LMC (Fukui et al. 1999, 2008), even this simple visual comparison implies a close relation between A_V and $I_{\rm CO}$ in the
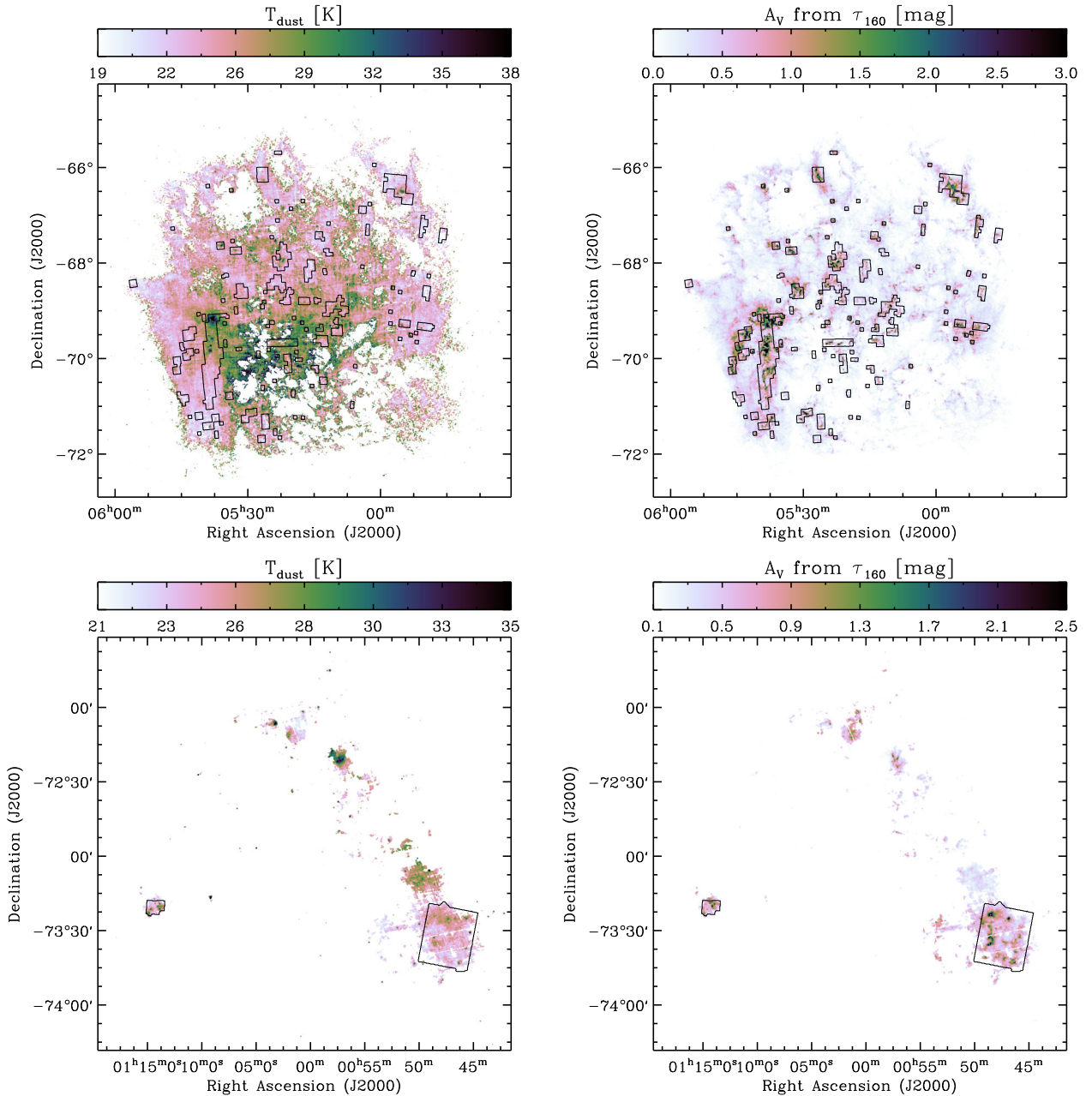

Figure 2. Dust temperature (left) and *A*$_V$ (right; from τ_{160}) maps of the LMC (upper panels) and SMC (lower panels). The fields covered by CO data are shown in black contours. In addition to the majority of bright CO, the MAGMA field (black contours in the LMC) also shows enhancement of visual extinction relative to other regions in the LMC. That is, there is already a 'by-eye' $I_{\rm CO}$–*A*$_V$ relation apparent in the figure. (A colour version of this figure is available in the online journal.)
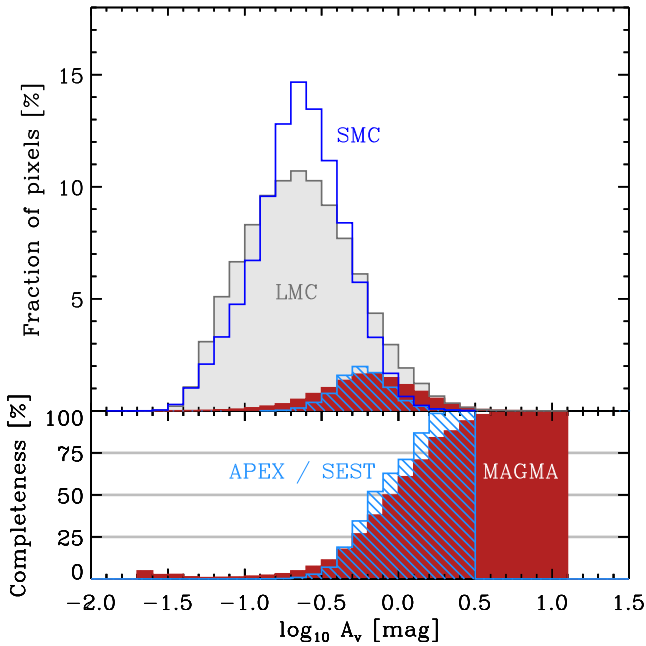
Figure 3. Top: histogram of A_V distribution in the LMC field (grey filled histogram; it includes all regions in the LMC with the *Herschel* IR intensities greater than their 3σ uncertainties) and the MAGMA field (red filled histogram; this is the region in the LMC field where the MAGMA survey mapped in CO). Likewise, the unfilled blue histogram shows distribution of A_V in the SMC field, and histogram shaded with blue diagonal lines shows that in the CO mapped regions in the SMC (the APEX and SEST fields). Low extinction ($A_V \leq 1$ mag) lines of sight dominate the Magellanic Clouds and also comprise a large portion of the CO mapped area in each galaxy. Bottom: completeness of A_V in the CO mapped regions in the Magellanic Clouds (shown as red filled histogram for the MAGMA field, and histogram shaded with blue diagonal lines for the APEX and SEST fields), calculated by dividing the number of pixels with a given A_V in the CO mapped region by the total number of pixels with that A_V in each galaxy. The completeness level drops to ≈ 50 per cent at $A_V \approx 0.8$ mag in the MAGMA field and at $A_V \approx 0.6$ mag in the APEX and SEST fields. (A colour version of this figure is available in the online journal.)

Magellanic Clouds. In Fig. 2, we also note a quite significant variation of dust temperature across the Magellanic Clouds. This reflects the variation of ISRF strength, which may impact the amount of CO emission in the region via photodissociation (e.g. Israel 1997). We further explore this idea in Section 3.3, where we divide the MAGMA field into high and low T_{dust} regions.

In Fig. 3, we show histograms of A_V distribution over the whole IR-bright area and specifically over the CO mapped regions in the LMC and SMC. The bottom panel shows the completeness of A_V coverage by the CO map in each galaxy, i.e. the fraction of LMC and SMC pixels in the specified A_V bin (bin size of 0.1 dex mag) that lie within each galaxy's CO map. Therefore, 100 per cent in the bottom panel means that all pixels in that A_V bin lie within CO map's field of view.

Low extinction ($A_V \leq 1$ mag) lines of sight make up most of the area in the Magellanic Clouds, even within the CO mapped regions where we observed enhanced dust shielding relative to other regions of the LMC and SMC in Fig. 2. On ~ 10 pc scale, the distribution of A_V in the MAGMA field is well described by a log-normal function with mean 0.65 mag and standard deviation 0.30 dex. The APEX and SEST fields in the SMC show a narrower A_V distribution, which can be fit by a log-normal function with mean 0.58 mag and stan-

dard deviation 0.17 dex. This is in qualitative agreement with the observations of local molecular clouds on sub-pc scale, where the column density distribution is well fit by a log-normal function, often accompanied by a power-law tail (Kainulainen et al. 2009). At matched spatial resolution, we will see that the average extinction through a local Milky Way cloud is ≈ 1–2 mag (Section 2.5.2), a few times higher than the mean A_V we see in the CO surveyed regions in the Magellanic Clouds. The A_V associated with a Milky Way cloud would thus represent a bright spot, but not a dramatic outlier, in the Magellanic Clouds on ~ 10 pc scale.

The completeness of the MAGMA coverage exceeds 50 per cent at $A_V \sim 0.8$ mag. That is, about one-half of the pixels in the LMC field with $A_V \sim 0.8$ mag lie within the MAGMA field. In the most extreme case where MAGMA recovers all of the CO emission from LMC then the bias in our I_{CO} estimate at a given A_V will simply be the completeness in that A_V range. So above ≈ 0.8 mag, completeness introduces no more than a factor of 2 uncertainty. In reality, MAGMA does not recover all CO emission from the LMC and we do not expect the measurement in the MAGMA field to be quite so strongly biased. In the SMC, the completeness of the APEX and SEST coverage becomes 50 per cent at lower A_V than MAGMA, at $A_V \sim 0.6$, which is expected since the SMC CO map covers a large contiguous area in the south-west of the SMC.

2.5 Milky Way comparison data

We compare the I_{CO}–A_V relation in the Magellanic Clouds to the Milky Way using three data sets: (1) analytic approximations to the highly resolved (sub-pc) I_{CO}–A_V relation measured in the Pipe nebula and Perseus molecular clouds; (2) observations of local molecular clouds degraded to ~ 10 pc resolution; and (3) the pixel-by-pixel relation for high Galactic latitude lines of sight also convolved to ~ 10 pc resolution.

2.5.1 Highly resolved Milky Way clouds

The proximity of Milky Way molecular clouds allows highly resolved comparisons of I_{CO} and A_V, with the limiting reagent mostly wide field CO maps. We are aware of two quantitative studies of the dependence of I_{CO} on A_V in nearby clouds: Lombardi et al. (2006) considered the Pipe nebula and Pineda et al. (2008) studied Perseus. Pineda et al. (2010) carry out a similar study of Taurus but do not analyse the relation in exactly the way we need for this comparison. These studies find

$$I_{\text{CO}} = \begin{cases} I_0((1 + e^{-k(A_V - A_V^{\text{mid}})})^{-1} - b): & \text{Pipe,} \\ I_0(1 - e^{-k(A_V - A_{k12})}): & \text{Perseus,} \end{cases} \quad (3)$$

where for Perseus I_0 is the integrated intensity at saturation, A_{k12} is the minimum extinction needed to get CO emission, and k is the conversion factor between the amount of extinction and the optical depth. In the Pipe, the relation looks similar, but here $I_0(1 - b)$ is the saturation intensity, and the minimum extinction required for CO emission is equals to $A_V \sim A_V^{\text{mid}} - \frac{1}{k} \ln \frac{1-b}{b}$. We list the best-fitting parameters[4] reported in the above studies for these clouds in Table 2

[4] Note that the best-fitting parameters for the Pipe nebula give negative minimum extinction threshold, which means that I_{CO} is positive at $A_V = 0$. These authors also fit I_{CO}–A_V relations for these clouds using a linear function (i.e. with the functional form $I_{\text{CO}} = A_{V0} + rA_V$, where A_{V0} is the minimum extinction threshold for CO emission and r is the linear coefficient relating

Table 2. $I_{\rm CO}$–A_V relation fitting parameters in the Pipe nebula and the Perseus molecular cloud.

Cloud	I_0 (K km s^{-1})	k (mag^{-1})	A_{k12} (mag)	$A_V^{\rm mid}$ (mag)	b
Pipe[a]	32.3	0.694	n/a	4.55	0.036
Perseus[b]	42.3	0.367	0.580	n/a	n/a

Notes. [a] $I_{\rm CO} = I_0((1 + {\rm e}^{-k(A_V - A_V^{\rm mid})})^{-1} - b)$: Lombardi et al. (2006). [b] $I_{\rm CO} = I_0(1 - {\rm e}^{-k(A_V - A_{k12})})$: Pineda et al. (2008).

and plot the two relationships as a point of comparison throughout the paper.

The qualitative behaviour of the relations observed in the Pipe and Perseus highlight some of the key physics governing CO emission from molecular clouds (e.g. classic PDR models such as Maloney & Black 1988; van Dishoeck & Black 1988). First, there appears to be a minimum amount of dust extinction required for bright CO emission. Below this level, CO abundance is very low because of photodissociation, leading to no or negligible CO emission. Above that threshold there is an approximately linear relation between A_V and $I_{\rm CO}$ for some range of A_V. Then at very high A_V, CO intensity saturates as the line becomes very optically thick across the whole velocity range. In this optically thick regime the observed CO intensity becomes a product of excitation temperature ($T_{\rm ex}$), the beam filling factor, and line width. While this observed dependence of $I_{\rm CO}$ on A_V highlight the importance of dust shielding for CO emission, the differences among the relation for the two clouds and even within an individual cloud make it clear that A_V is not the only factor that determines the amount of CO emission. Different geometries and environmental factors (external radiation field, density structure, internal heating) will lead to a substantial dispersion in CO emission even for the same amount of shielding. Indeed, one of the main conclusions of Pineda et al. (2008) was that environmental effects can be very strong even within the same molecular cloud complex (e.g. see their fig. 6).

2.5.2 *Integrated measurements for Milky Way clouds*

To make a more direct comparison of the Milky Way to the Magellanic Clouds, we consider local Galactic molecular clouds from table 1 in Dame et al. (2001). We calculate their average A_V and $I_{\rm CO}$ values on ∼10 pc scales to simulate how they might appear in one of our Magellanic Cloud maps and report the measurements in Table 3. We compile the A_V and $I_{\rm CO}$ values of these clouds from the Milky Way CO map by Dame et al. (2001) and the $E(B - V)$ map published by the *Planck* collaboration (Planck Collaboration XI 2014), where we take $R_V = 3.1$ to convert $E(B - V)$ into A_V. We refer the interested reader to Planck Collaboration XI (2014) for more detailed information on the *Planck* $E(B - V)$ map and note that A_V in local molecular clouds calculated from the *Planck* $E(B - V)$ map may be slightly overestimated.[5]

To simulate the ∼10 pc physical resolution of our Magellanic Cloud data, we convolve the *Planck* A_V map (original resolution 5 arcmin) and the Dame et al. (2001) CO map (original resolution 7.5 arcmin) with a 3° Gaussian kernel. At 200 pc, a typical distance to a nearby molecular cloud, this resolution corresponds to ≈10.5 pc. Most local clouds subtend several pixels at this resolution (7 pixels for the Chamaeleon molecular cloud at the least; at the most 313 pixels for the Taurus–Perseus–Auriga complex). We take the median A_V and $I_{\rm CO}$ across all of these pixels as representative and report them in Table 3; we adopt the A_V and $I_{\rm CO}$ of each cloud at ±1σ percentiles as the representative uncertainties when plotting the data.

2.5.3 *High galactic latitude (|b| > 5°) emission*

As a final point of comparison, we use all-sky Milky Way CO and A_V maps to explore the high Galactic latitude lines of sight. We use the same *Planck* $E(B - V)$ map[6] described above section to calculate A_V. Because the Dame et al. (2001) CO map only covers limited range of Galactic latitudes ($|b| < 30°$), we use the *Planck* TYPE 2 CO map. This is a map of integrated CO line emission that has been extracted from the *Planck* High Frequency Instrument (HFI) channels using the multichannel method by the *Planck* team (Planck Collaboration XIII 2014). This map has an angular resolution of 15 arcmin, and is known to be better suited for intermediate/high Galactic latitude regions than the TYPE 1 CO map (Planck Collaboration XIII 2014).

Before comparing this map with the A_V map, we corrected for the contribution of ^{13}CO to the map by dividing the TYPE 2 CO map by 1.2. We then degraded the resolution of the CO map to match that of the A_V map. Using the A_V and CO maps described above, we construct a pixel-by-pixel $I_{\rm CO}$–A_V relation for the high-latitude Milky Way sky suitable for comparison to Magellanic Cloud measurements. We consider all area with $|b| > 5°$, avoiding the Milky Way midplane in order to remove confusion from multiple components along a line of sight.

3 RESULTS

3.1 $I_{\rm CO}$ versus A_V in the Magellanic Clouds

Figs 4 and 5 show our main observational results, the $I_{\rm CO}$–A_V relationship in the Magellanic Clouds. For this analysis, we consider the MAGMA field for the LMC and the APEX field for the SMC. For the APEX CO data, we assume a ratio of unity to translate CO $J = 2 \rightarrow 1$ to CO $J = 1 \rightarrow 0$ (e.g. see Bolatto et al. 2003). For clarity, the $I_{\rm CO}$-A_V relationship in the N83 complex is not displayed in Figs 4 and 5, but we note that it is similar to the $I_{\rm CO}$-A_V relationship in the southwest region of the SMC.

Fig. 4 shows the relationship between $I_{\rm CO}$ and A_V pixel-by-pixel for each galaxy (the LMC in upper panels and the SMC in lower panels). The distribution of individual data points is shown as the contours and grey points in the left-hand panels (semi-log scale).

A_V and $I_{\rm CO}$), and in this case the minimum extinction threshold for CO emission in the Pipe nebula is positive.

[5] The *Planck* $E(B - V)$ map used in this analysis is a conversion of their dust optical depth (τ) to $E(B - V)$ using the correlation between $E(B - V)$ of SDSS quasars and dust optical depth at high Galactic latitude lines of sight (i.e. the conversion we discussed in Section 2.3.2, see fig. 22 in Planck Collaboration XI 2014). However, Planck Collaboration XXV (2011) compared column density N(H) from NIR extinction with dust optical depth, finding higher dust emissivity, τ/N(H), in the molecular phase by a factor of

∼2 than the atomic phase (see also fig. 20 in Planck Collaboration XI 2014). Therefore, we caution that the *Planck* $E(B - V)$ map may systematically overestimate the actual $E(B - V)$ (and A_V) in local clouds. For example, comparison of $E(B - V)$ from NIR extinction and the *Planck* $E(B - V)$ map in Taurus and Ophiuchus molecular clouds (Planck Collaboration XI 2014) shows that correlations between them are pretty strong (their table 5), but the *Planck* $E(B - V)$ is systematically higher by 25 per cent.

[6] Unlike the case for the local clouds, high Galactic latitude lines of sight are diffuse and the application of $E(B - V)/\tau$ conversion is not expected to overestimate the actual $E(B - V)$ value in this case.

Table 3. Median A_V and I_{CO} of Galactic molecular clouds at 3° resolution.

Cloud	l^a (°)	b^a (°)	Area^a (deg^2)	Pixels	$\langle A_V \rangle^b$ (mag)	$\langle I_{CO} \rangle^c$ (K km s^{-1})	$\langle I_{CO}/A_V \rangle^{b,c}$ (K km s^{-1} mag^{-1})
Aquila	20	8	227	85	4.0	7.5	2.0
Camelopardalis	148	20	159	61	0.54	0.32	0.55
Chamaeleon	300	−16	27	7	1.4	2.0	1.6
Gum Nebula	266	−10	97	37	1.5	0.46	0.31
Ophiuchus	355	17	422	151	1.9	2.6	1.3
Orion	212	−9	443	163	2.1	1.6	0.65
Polaris Flare	123	24	134	55	0.81	2.5	2.7
Taurus	170	−15	883	313	1.9	3.5	1.8

Notes. ^{a}Compiled from table 1 in Dame et al. (2001).
^{b}Computed from *Planck E(B − V)* map, assuming $R_V = 3.1$. Note that this A_V may be systematically overestimated (see text).
^{c}Computed from Dame et al. (2001) CO map.

The median and 1σ scatter of the data are shown as the red circles (binned by log A_V) in both the left- (semi-log scale) and right-hand (log scale) panels. In the left-hand panel of Fig. 4, we find that the I_{CO}–A_V relation for individual lines of sight shows large scatter, but the median trend (red circles) confirms the impression from simple visual comparison in Fig. 2. That is, the CO intensity appears to increase as a function of A_V in the Magellanic Clouds.

In Fig. 5, we plot this average relation for both galaxies. Here the mean and uncertainty derive from Monte Carlo simulation (Section 2.3.3), so that the error bars reflect the uncertainty in the mean across 1000 realizations for the LMC and an equivalent uncertainty for the SMC. These average relations in Fig. 5 are thus our best estimate of how CO intensity (I_{CO}) depends, on average, on dust shielding (A_V) at cloud-scales in the LMC and SMC. The estimate takes into account the systematic uncertainties in estimating A_V from the IR emission. Interpreting the error bars requires some care; many of the factors that we simulate create correlated errors across a whole realization. Therefore one should largely view the error bars as the space within which the mean relation could move.

Care must also be taken when interpreting the high A_V portion of the average relations. Recall that low A_V ($A_V \leq 1$) dominate the Magellanic Clouds, and there are very few data points in the high A_V bins in the LMC and SMC (e.g. see Fig. 3). For example, there are only 15 lines of sight that have A_V greater than 10 in the LMC, and no line of sight has A_V greater than 4 in the SMC. The greater number of points at lower A_V will lead those points to preferentially scatter to high A_V and contaminate the measurements at high A_V in the Monte Carlo calculation. This will artificially lower the mean I_{CO} at high A_V in the Monte Carlo simulation.

With this in mind, we note that except at $A_V \geq 4$ in Fig. 5, the LMC and SMC in Figs 4 and 5 overlap one another, showing similar CO intensity at a given A_V. This agreement between the LMC and SMC despite their factor of ≈2 difference in metallicity is consistent with the theoretical picture that CO intensity depends on dust shielding (A_V) in an approximately universal way. In the next section, we will compare the Magellanic Clouds to the Milky Way in several ways to see that this holds true from $Z \approx 1/5 \, Z_\odot$ up through solar metallicity.

We noted earlier that the measured I_{CO} scatters considerably at a given A_V in Fig. 4. Much of this scatter reflects the noise in the CO map, and this scatter clearly dominates the distribution of individual data below $A_V \approx 1$ mag. Still, we verified that a real CO signal emerges as we stack the CO spectra in the LMC in bins of A_V (see Fig. B1). At higher extinctions, $A_V \geq 1$ mag, we also see substantial additional scatter about the median CO intensity in fixed

A_V bins. We interpret this as real astronomical signal, indicating that line of sight A_V on 10 pc scale is not a perfect predictor of I_{CO} even in the absence of noise. This is reasonable and expected as many physical effects beyond shielding may influence CO emission, for example, variations in cloud structure, geometry, chemistry, and the ISRF. The important caveat to bear in mind is that while I_{CO} does depend on A_V, *the relationship emerges only after substantial averaging* because individual lines of sight have large scatter in I_{CO}–A_V parameter space.

3.2 Comparison to the Milky Way

We are primarily interested in testing the hypothesis that CO emission depends on dust shielding (A_V) in the same manner across environment that differ in metallicity. In the previous section, we saw that CO intensity at a given A_V is indeed similar in the LMC and SMC. In this section, we compare our Magellanic Cloud results to the Milky Way in three different ways.

First, we compare the Magellanic Clouds to the highly resolved (sub-pc resolution) I_{CO}–A_V relation measured in the Pipe nebula and Perseus molecular clouds. These appear as the dashed line (Pipe) and the dash–dotted line (Perseus) in Figs 4 and 5. Overall, the I_{CO}–A_V relation in the Magellanic Clouds resemble that in the Pipe nebula (note that the Pipe curve is not a fit to our data or even normalized to match our data), while the Magellanic Clouds exhibit 2–3 times fainter CO emission than the Perseus molecular cloud at high A_V. Most importantly, neither the LMC nor the SMC in Fig. 4 exhibits the qualitative features observed in the Pipe and Perseus (Section 2.5.1), at least not prominently. We observe no clear saturation in I_{CO} and the threshold behaviour, if present, appears far weaker than in the Perseus molecular cloud. The average I_{CO}–A_V relations in Fig. 5 seem to exhibit a saturation of CO at high A_V ($A_V \geq 10$ mag for the LMC, $A_V \geq 4$ for the SMC), but as noted earlier, the apparent trends observed at high A_V in the average I_{CO}–A_V relations are vulnerable to artefacts arising from Monte Carlo simulation.

The lack of evidences for the saturation of CO and threshold behaviour in the Magellanic Clouds almost certainly stem from the dramatic difference in resolution between our measurement in the Magellanic Clouds and those used to construct the Pipe and Perseus curves. Our measurements combine large parts of a cloud (∼10 pc) into a single data point, so that each line of sight is an average of A_V and I_{CO} in a 10-pc beam. On the other hand, the Pipe and Perseus relations are measured at much higher resolution (sub-pc). These clouds would not exhibit $A_V \sim 5$–10 mag at 10 pc resolution. For a
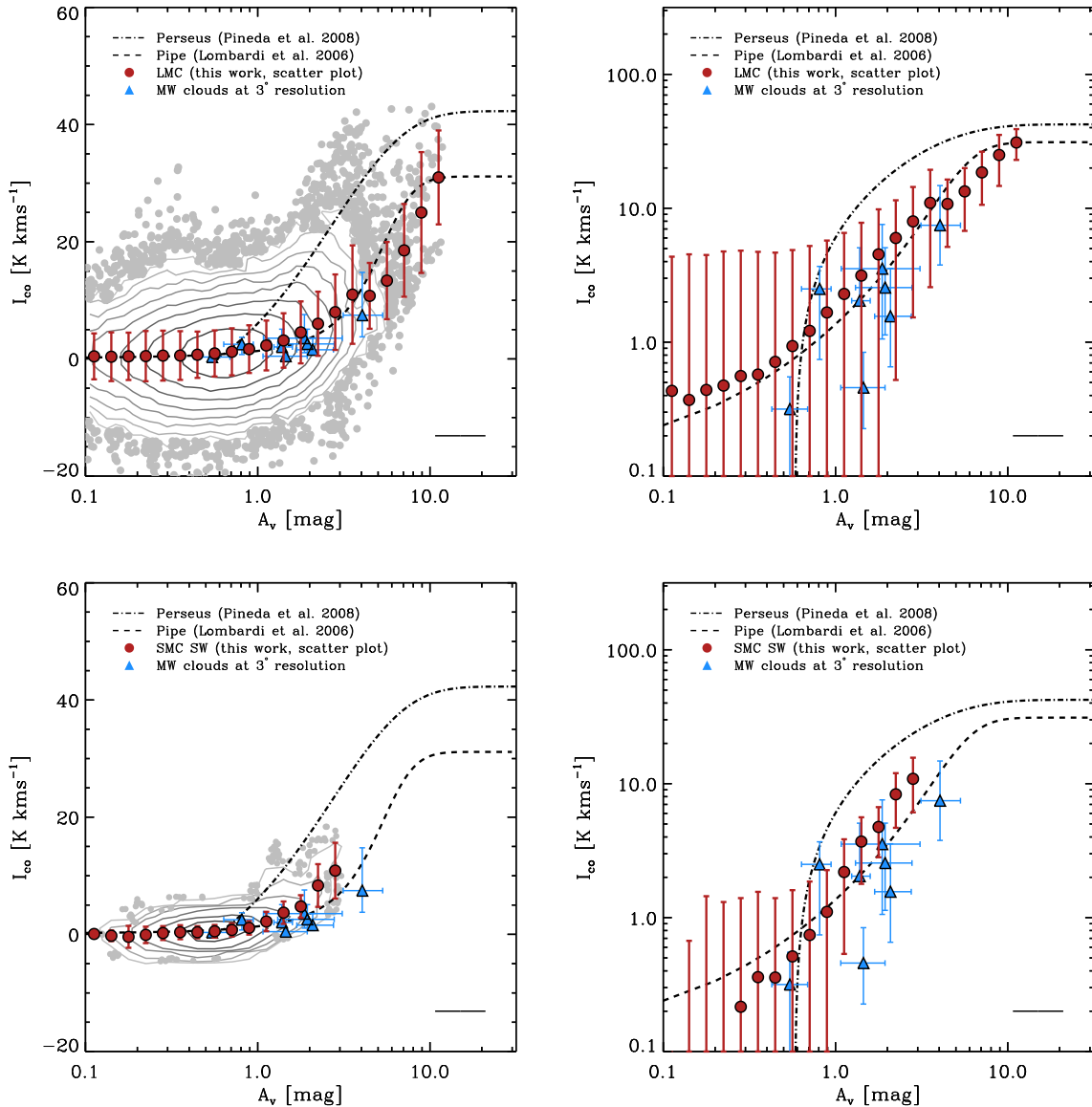
Figure 4. Pixel-by-pixel comparison of A_V (x-axis) and I_{CO} (y-axis) in the LMC (top panels) and SMC (bottom panels), shown in semi-log scale in the left-hand panels and in log scale in the right-hand panels. In the left-hand panels, the distribution of data points in the LMC and SMC is shown as the contours, while the grey points show individual lines of sight where the density falls below 10 points per bin. The lowest contour means there are at least 10 individual data points in the bin, increasing by factors of 2 with each step for the LMC and by factors of 3 for the SMC. The red circles with error bars indicate the median CO intensity and its scatter measured in bins of log A_V, our LMC and SMC I_{CO}–A_V relations. For comparison, we also plot the I_{CO}–A_V relations measured at much higher (∼sub-pc) resolution for two Galactic clouds, Perseus (dash–dotted; Pineda et al. 2008) and the Pipe (dashed; Lombardi et al. 2006). Blue triangles represent a more well-matched Milky Way comparison, Galactic molecular cloud data compiled from *Planck* (Planck Collaboration XI 2014) and Dame et al. (2001), degraded to physical resolution similar to what we achieve in the Magellanic Clouds (3°, which corresponds to ∼10.5 pc at the distance of 200 pc). In the semi-log plots one can see how median CO intensity approach zero as A_V decreases in the Magellanic Clouds, while in the log–log plots we rescale the y-axis to better compare I_{CO}–A_V relations in the Magellanic Clouds with Galactic molecular clouds. The horizontal error bar in the bottom right-hand corner of each panel shows a typical uncertainty in A_V derived from Monte Carlo analysis (Section 2.3.3). (A colour version of this figure is available in the online journal.)

fairer comparison to these highly resolved curves, one would need very high resolution A_V and I_{CO} data in the Magellanic Clouds.

An alternative approach is to measure A_V and I_{CO} averaged over a 10-pc beam for the local clouds. These appear as blue triangles in Figs 4 and 5. These triangles represent our best estimate of how local clouds would look like at the distance of the Magellanic Clouds. This makes them analogous to the individual grey points in Fig. 4. At matched ∼10 pc resolution, most of the Milky Way clouds have rather low A_V, ranging from ∼0.5 to ∼4.0 mag. The agreement

between the Milky Way and the Magellanic Clouds is much better in the case of matched resolution than for the highly resolved Milky Way relations. A close inspection of Fig. 5 suggests that some of the local clouds have rather fainter CO emission at a given A_V than the average lines of sight in the Magellanic Clouds, but this could be partly due to overestimated A_V in the local clouds in the *Planck* maps (Section 2.5.2). Given that the scatter in I_{CO} is very large at a given A_V both for the Magellanic Clouds and the Milky Way clouds, we interpret the integrated measurements of I_{CO}–A_V in local clouds
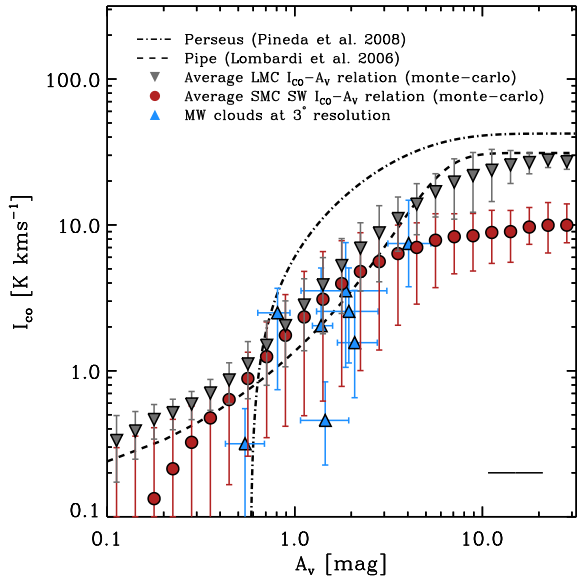
Figure 5. Average I_{CO}–A_V relation in the LMC (grey downward triangles) and SMC (red circles) from Monte Carlo simulation (Section 2.3.3). Other lines and symbols are the same as Fig. 4. Here, the vertical error bars associated with the average relations do represent uncertainty in the average relations. Note that high A_V points in the average relations arise from very few lines of sight moving across A_V bins as we simulate A_V maps and thus mimic saturation effect observed in highly resolved Galactic molecular clouds (see Section 2.5.1). The agreement between the LMC, SMC, and integrated measurements for the Milky Way is fairly good at $A_V \leq 4$, suggesting that dust shielding is the primary factor that determines the distribution of bright CO emission from a molecular cloud. (A colour version of this figure is available in the online journal.)

to substantially agree with our measurements in the Magellanic Clouds. This reinforces our results from the internal comparison of the two Magellanic Clouds.

As a final comparison, we plot the I_{CO}–A_V relation for high-latitude ($|b| > 5°$) Milky Way lines of sight in Fig. 6. The high-latitude Milky Way lines of sight (black triangles) exhibit a similar shape to the Magellanic Cloud relations but with a tendency towards lower I_{CO} at a given A_V. That is, the Magellanic Clouds appear to be brighter than the high-latitude Milky Way in CO on average for a given A_V. Quantitatively, the median I_{CO}/A_V for Milky Way high-latitude lines of sight is ≈ 0.5 K km s^{-1} (mag)$^{-1}$, which is about 0.25 times the value for the LMC [≈ 1.9 K km s^{-1} (mag)$^{-1}$].

Our best explanation for this difference is that the Milky Way values are likely to be biased low by dust associated with a long path length through the Milky Way H I disc. For example, at $b \sim 10°$ a 200 pc thick H I disc will yield an integrated path length of roughly a kpc. This path length will preferentially sample atomic gas, which has a higher scale height than molecular gas and little associated CO emission. More, the dust along that line of sight through and extended disc will contribute little to shielding distant CO from dissociating radiation. Such effects will undermine any mapping between line of sight extinction and the local dust shielding that should affect CO emission. In Appendix A2, we show that a simple correction for dust associated with an extended H I disc leads to a median I_{CO} at a given A_V for the high-latitude Milky Way that more closely resembles what we find in the Magellanic Clouds.

The Magellanic Cloud data may also be biased high by our focus on the CO mapped regions. As shown in the bottom panel of Fig. 3, the completeness of A_V in the MAGMA field drops to ~ 50 per cent
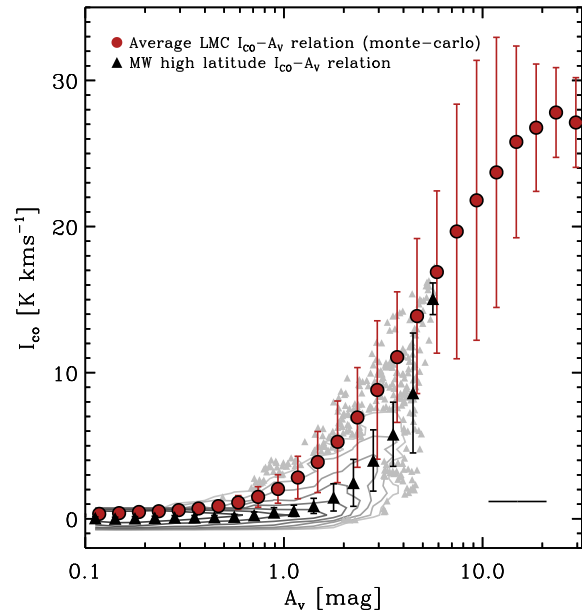

Figure 6. Integrated CO intensity (*y*-axis) as a function of A_V (*x*-axis) at high Galactic latitude ($|b| > 5°$) lines of sight in the Milky Way, compiled from *Planck* data (Planck Collaboration XI 2014) degraded to $\sim 3°$ resolution. The contours and grey points show the distribution of data points in the I_{CO}–A_V space, following the same contour definition for the LMC in the left-hand panel of Fig. 4. The median CO intensity at a given A_V is shown as the black triangles, and the average LMC I_{CO}–A_V relation (Fig. 5) is shown as the red circles, shifted slightly towards right in *x*-axis for easier comparison. (A colour version of this figure is available in the online journal.)

at $A_V \sim 0.8$ mag, and at $A_V \sim 0.6$ mag in the APEX and SEST fields. This means that at $A_V \sim 0.8$ mag, I_{CO}/A_V in the LMC has a lower limit of about half the current value if we assume that the other half lines of sight not mapped in CO do not have associated CO emission at all, and a similar logic can be applied to the SMC as well. If this is the case, I_{CO} at a given A_V would be closer between the Magellanic Clouds and high-latitude Milky Way. Even if this bias drives the results, Fig. 6 suggests the somewhat surprising result that the active parts of the Magellanic Clouds are better at emitting CO than the high-latitude Milky Way.

Overall, the sense of the comparison made in Section 3.2 is this: the Magellanic Clouds, at least the bright regions covered by CO surveys, show I_{CO} at a given A_V comparable to or somewhat below than those found at highly resolved (sub-pc) local Galactic clouds. The Magellanic Clouds data do not show clear evidence for saturation of CO line and A_V threshold observed in high-resolution Milky Way data, likely due to low resolution. After accounting for resolution differences, we find that a sample of Milky Way clouds at 10 pc resolution largely overlaps the average I_{CO}–A_V relations in the Magellanic Clouds. Taking a broader view and considering high-latitude emission from the Milky Way, we find a qualitatively similar I_{CO}–A_V relation to the Magellanic Clouds but note important quantitative differences with the sense that at a fixed A_V, gas in the high-latitude Milky Way emits somewhat less CO than the regions covered by the CO maps in the Magellanic Clouds.

3.3 Influence of the interstellar radiation field

Fig. 4 showed large scatter in I_{CO} at fixed A_V, implying additional physics beyond the abundance of dust at play. One simple and often discussed 'second parameter' is the ISRF (Israel 1997; Pineda et al.
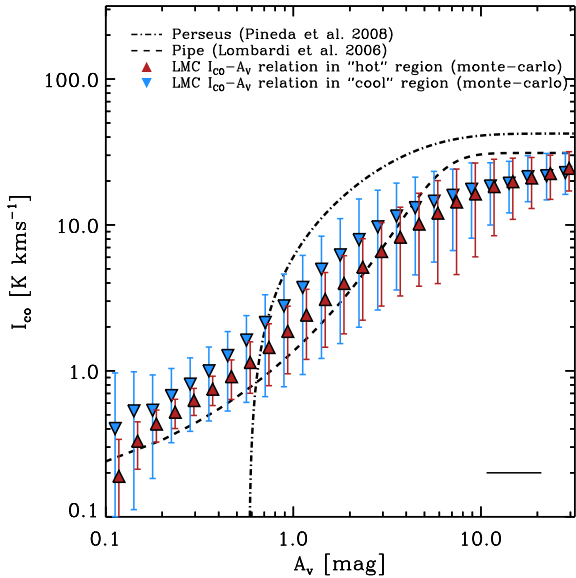
Figure 7. Temperature dependence of LMC I_{CO}–A_V relation. We divide the MAGMA field into hot ($T_{dust} > 24.1$ K; the red upward triangles with error bars, shifted slightly towards right in x-axis for easier comparison) and cool ($T_{dust} < 24.1$ K; the blue downward triangles with error bars) regions based on the median dust temperature ($\sim$24.1 K). Interestingly, the region with hotter dust temperature (and more intense ISRF) shows fainter CO emission measured at a fixed dust shielding (A_V) compared to the region with colder dust temperature. This is the opposite of what one would expect for the region with hotter dust temperature having stronger CO emission due to a higher kinetic temperature, and we interpret this as the evidence for an intense ISRF to suppress CO emission at a fixed dust shielding in the hot region more than the cool region. (A colour version of this figure is available in the online journal.)

2009). We have estimated this quantity as part of our dust modelling: the dust temperature, T_{dust}, depends on the strength of ISRF such that $X_{ISRF} \sim T_{dust}^{4+\beta}$). The radiation field drives the photodissociation of CO molecules, so that we may reasonably expect T_{dust} to affect I_{CO} within a bin of fixed A_V.

Fig. 7 shows a simple test for the effect of T_{dust} as a second parameter (as an extension to this test, we also discuss the effect of strong radiation field on the I_{CO}–A_V relation in Appendix A3, by focusing on 30 Doradus complex in the LMC). For this experiment, we divide our LMC data into two bins: a 'cool' region with lower than median T_{dust}, i.e. $T_{dust} < 24.1$ K, and a 'hot' region with higher than median T_{dust}, $T_{dust} > 24.1$ K (see Fig. 2 for the dust temperature map). The median dust temperatures of these two regions are $\sim$26.0 K ('hot') and $\sim$22.7 K ('cool'). With our fiducial $\beta = 1.5$, this temperature difference corresponds to difference in ISRF strength of a factor of $\sim$2.1. Note that the ISRF in the MAGMA field is already on average greater by a factor of $\sim$5.8 than the solar neighbourhood, where $T_{dust} \sim 17.5$ K. We calculate the average I_{CO}–A_V relations in the 'hot' and 'cool' regions and estimate their uncertainties using Monte Carlo simulation.

Interestingly, Fig. 7 shows that I_{CO} at fixed A_V is higher in the cool region (blue downward triangles) than the hot region (red upward triangles) in the MAGMA field. This observed trend supports the idea that an intense ISRF suppresses CO emission, since several effects might lead to the opposite direction of what we see in Fig. 7. First, the uncertainties on τ_{160} and T_{dust} are correlated in the sense that underestimating T_{dust} would lead us to overestimate τ_{160}. This

has the opposite sense of what we see here and so seems unlikely to drive the separation in Fig. 7. Second, if a higher ISRF leads to higher excitation for the CO, we might expect a higher brightness temperature in regions with high T_{dust}. Again, this has the opposite sense of the separation we observe. A correlation between T_{dust} and β might produce some of the signal we see, but such correlations are notoriously difficult to verify (Shetty et al. 2011). The simplest explanation of Fig. 7 is that an intense ISRF tends to suppress CO emission at a fixed dust abundance, presumably due to enhanced dissociation of CO. Enhanced dissociation of CO under a strong ISRF then would lead to reduced area of CO photosphere, likely causing more beam dilution and decreased integrated CO intensity. This agrees with the results of Israel (1997), who use dust emission as a tracer of H_2 column density to calculate X_{CO}, and find that X_{CO} increases as a function of the strength of ISRF. On the other hand, this disagrees with studies focused on giant molecular cloud (GMC) properties measured from CO emission (Pineda et al. 2009; Hughes et al. 2010), which find no apparent dependence of the properties of CO clumps or X_{CO} on the strength of radiation field.

3.4 Median I_{CO}/A_V across different environments

As a summary of our main results, we compile the median I_{CO}/A_V values across different environments at matched resolution in Table 4. In the MAGMA field, the median I_{CO}/A_V is $\approx$1.9 K km s^{-1} (mag)$^{-1}$. We find slightly lower values in the APEX field and the SEST field in the SMC, with the median I_{CO}/A_V varies from 1.1 to 1.5 K km s^{-1} (mag)$^{-1}$ depending on which transition of CO line to use in the calculation. The median I_{CO}/A_V value for local clouds at matched resolution is $\approx$1.3 K km s^{-1} (mag)$^{-1}$. The lower I_{CO}/A_V in the integrated measurements of local clouds partly arises from overestimation of A_V in these clouds in the *Planck* data (see Section 2.5.2). Also, we note that calculating a median value is sensitive to the area in which the calculation is made and that cloud boundaries are not known with precision. If our adopted cloud areas (Table 3) are too large then they may bias the local cloud measurements somewhat low. As discussed in Section 3.2, the median I_{CO}/A_V in Milky Way high-latitude lines of sight is significantly lower than the LMC and SMC, but a correction for contamination by an extended H I disc (see Appendix A2 for details) bring these values into closer agreement.

For comparison, we also recast Galactic CO-to-H_2 conversion factor ($X_{CO} = 2 \times 10^{20}$ cm^{-2} (K km s^{-1})$^{-1}$; Bolatto et al. 2013)

Table 4. Median I_{CO}/A_V values across environments.

Galaxy	Region	$\langle I_{CO}/A_V \rangle^a$ (K km s^{-1} mag^{-1})
LMC	MAGMA field	1.9
	Hot	1.5
	Cool	2.2
Milky Way	High latitude, without H I correction	0.5
	High latitude, with H I correction	0.8
	Local clouds from *Planck*	1.3
	Standard X_{CO}	4.7
SMC	APEX field (CO $J = 2 \rightarrow 1$)	1.1
	SEST field (CO $J = 2 \rightarrow 1$)	1.5
	SEST field (CO $J = 1 \rightarrow 0$)	1.4

Note. ^{a}We caution that these values are very sensitive to the choice of pixels for computing the values, baseline correction for CO emission in the case of the LMC, and uncertainties associated with deriving A_V from IR emission.

into these units. One can calculate the corresponding I_{CO}/A_V for a standard X_{CO}, ≈ 4.7 K km s^{-1} (mag)$^{-1}$, by adopting a Galactic dust-to-gas ratio (N(H) $= 5.8 \times 10^{21} E(B - V)$; Bohlin et al. 1978) and $R_V = 3.1$. Unlike the rest of the median I_{CO}/A_V values, the recast of X_{CO} only considers molecular gas in the denominator and therefore represents an upper limit to the number that would be measured for a real cloud.

4 DISCUSSION

Our comparison of the Magellanic Clouds to the Milky Way argues that on ~10 pc scales CO intensity tracks dust column density, expressed as A_V. A logical corollary, though one we cannot prove with existing data, is that perhaps I_{CO} depends on A_V within clouds in an approximately universal way, at least when averaged over a sizable population of clouds. If this is the case, then the integrated CO emission from clouds, and by extension the CO-to-H$_2$ conversion factor, may be thought of as a problem with several separable parts. First, the distribution of A_V within a cloud will depend on the distribution of gas surface densities combined with the dust to gas ratio. Second, the CO emission from the cloud will depend on the A_V distribution. In the case where we are interested in the CO-to-H$_2$ conversion factor, the dust-to-gas ratio and surface density PDF will also determine what part of the cloud is H I and what part of the cloud is H$_2$. In this simplified view, the CO emission emerging from a whole cloud can be expressed as

$$I_{CO} = \int_{\Sigma_H} f^{CO,A_V} \left(DGR \times PDF(\Sigma_H) \right), \tag{4}$$

where Σ_H is the column density of hydrogen gas, PDF(Σ_H) is the distribution function for gas column densities in the cloud, DGR is the dust-to-gas ratio, which translated a value of Σ_H into A_V, and f^{CO,A_V} is the function that translates a value of A_V into a CO intensity. Here the integral is over all values of Σ_H and PDF should formally be the total column density per differential column density bin.

If one is interested in the CO-to-H$_2$ conversion factor rather than the total CO intensity, then the

$$X_{CO} \propto \frac{I_{CO}}{N_{H_2}} \approx \frac{\int_{\Sigma_H} f^{CO,A_V} \left(DGR, \Sigma_H \right)}{\int_{\Sigma_H} f^{H_2} \left(\Sigma_H, DGR \right) PDF \left(\Sigma_H \right)}. \tag{5}$$

Here the top integral is as above. The bottom integral sums the total H$_2$ mass in the cloud and includes the function $f^{H_2} (\Sigma_H, DGR)$, which indicates whether at the specified DGR gas of column density Σ_H is atomic or molecular.

This very simplified view breaks the CO-to-H$_2$ conversion factor into four parts: the distribution of gas column densities in a cloud; the dust-to-gas ratio; the relationship between CO and dust shielding; and the dependence of the H$_2$/H I transition on A_V. The benefit of stating the problem in this simplified way is that each of these topics has been studied independently (see the Introduction). The last few years have seen substantial work characterizing the column density distribution of local clouds. Theoretical work has also established a lognormal distribution as the baseline expectation for a turbulent cloud. Substantial recent theoretical work has also gone in to understanding the H I–H$_2$ transition. Finally, both theoretical and observational efforts (including Section 3) have been made to understand the dependence of I_{CO} on A_V. That is, this approach breaks the topic of CO emission from clouds in galaxies into a separable problem whose parts may be more tractable than the topic considered as a whole.
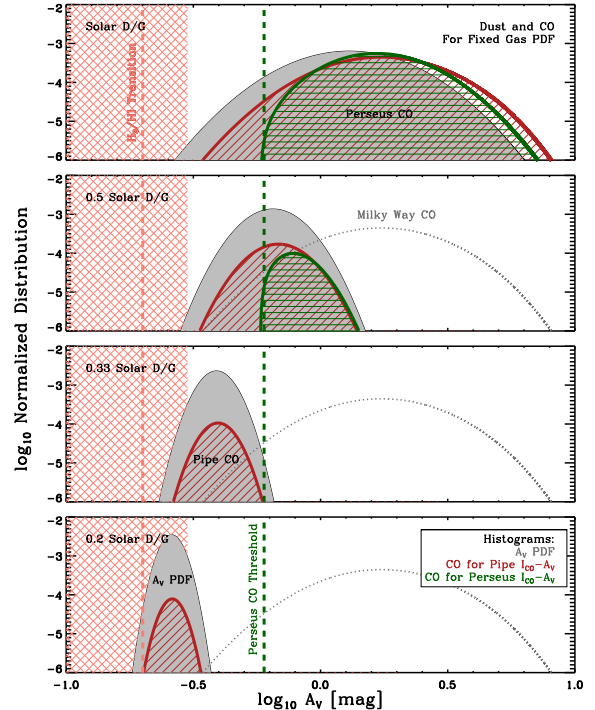

Figure 8. Illustration of our PDF-based calculation of X_{CO}. The grey filled histogram shows the same gas column density PDF at a range of dust-to-gas ratios. The hatched histograms indicate the implied distributions of CO intensity for each of these A_V distributions given the Pipe (red diagonal pattern) and Perseus (green horizontal pattern) I_{CO}–A_V relations. The light red cross hatched region at $A_V \leq 0.3$ shows where the transition between H$_2$ and H I will be important. The qualitative difference between Perseus and the Pipe is driven by the threshold in the Perseus I_{CO}–A_V relation, which we illustrate with a green dashed line. (A colour version of this figure is available in the online journal.)

4.1 Implications for the metallicity dependence of X_{CO}

This sketch can be used to make an empirically driven prediction for the metallicity dependence of the CO-to-H$_2$ conversion factor, X_{CO}. If we consider the column density distribution of gas to be universal, then the distribution of A_V is the dust-to-gas ratio times this column density distribution. This A_V distribution predicts the emergent CO emission from the cloud. The conversion factor depends on the ratio of this CO emission to the sum of the distribution of gas over the part of the cloud that is molecular. Then by varying the dust-to-gas ratio and repeating the calculation we can derive how X_{CO} changes as a function of DGR in this simple cartoon.

Schematically, Fig. 8 shows this approach. In this cartoon, gas obeys a universal PDF (here a lognormal), which is scaled by a dust to gas ratio to yield a PDF of A_V values for each cloud. That PDF appears as a grey normalized histogram. Applying a A_V-based prediction for I_{CO}, one arrives at a prediction for the CO intensity. That appears in red and green here for two such functions: the Pipe and the Perseus relation. This emission would be summed to get the integrated emission from the cloud. Finally, some part of the cloud is atomic (shown by the light red region) and that is not book-kept in the sum of the molecular mass.

To carry out the calculation quantitatively, we use the parametrization of A_V PDFs for local clouds at solar metallicity listed in table 1 of Kainulainen et al. (2009). In this analysis, we only consider the log-normal part of the A_V PDFs (i.e. ignoring the power-law tail). We also ignore $A_V \leq 1$ mag in the solar

metallicity clouds because the uncertainty in the extinction mapping used to derive the cloud PDFs becomes substantial below $A_V \sim 1$ mag (though note that the cartoon in Fig. 8 does show lower A_V in the top panel; this is just illustrative). These lognormal distributions clipped at $A_V > 1$ mag are our baseline gas distributions. That is, we consider the gas column density PDF to be

$$\text{PDF}\left(\Sigma_{\text{H},i}(\text{Z}_\odot)\right) = \frac{\text{PDF}\left(A_{V,i}(\text{Z}_\odot)\right)}{\text{DGR}(\text{Z}_\odot)}, \tag{6}$$

where the subscript i refers to one of the Kainulainen et al. (2009) A_V PDFs and $\text{DGR}(\text{Z}_\odot)$ is the solar metallicity dust-to-gas ratio. Because we make a relative calculation of X_{CO}, the numerical value of $\text{DGR}(\text{Z}_\odot)$ will cancel out of our results.

Without specifying what, precisely, DGR is for the Milky Way, we can scale these Milky Way PDFs to those we would expect for otherwise identical clouds at some fraction of solar metallicity by simply dividing values of A_V by the relative dust-to-gas ratio. That is, by dividing all A_V values by 2, we can shift the PDF to represent an otherwise identical cloud at half solar DGR. That is, we hold $\text{PDF}(\Sigma_{\text{H},i})$ fixed across metallicity and derive $A_{V,i}(Z)$ for some subsolar metallicity, Z, via

$$\begin{aligned}\text{PDF}\left(A_{V,i}(Z)\right) &= \frac{\text{DGR}(Z)}{\text{DGR}(\text{Z}_\odot)}\text{PDF}\left(A_{V,i}(\text{Z}_\odot)\right) \\ &\approx \frac{Z}{\text{Z}_\odot}\text{PDF}\left(A_{V,i}(\text{Z}_\odot)\right).\end{aligned} \tag{7}$$

In the last step, we take Z and DGR to vary linearly with one another, but a more complicated dependence (e.g. see Rémy-Ruyer et al. 2014) could easily be introduced into the formulae. Also note that at $Z < \text{Z}_\odot$, we will include $A_V < 1$ mag in our calculation; the uncertainty surrounding low A_V is in the determination of the Milky Way cloud PDFs, not in their inclusion in the calculation.

Next, we translate each A_V PDF into a predicted CO intensity. To do, we input the A_V distribution to one of the I_{CO}–A_V relationships discussed in the first part of the paper. In this calculation, we consider four relations: the Pipe; the Perseus; the LMC; and the high-latitude Milky Way. For the former two we use the best-fitting functions in Table 2. For the latter two we fit polynomial functions to the average I_{CO}–A_V relations for the LMC and Milky Way high-latitude lines of sight (red circles and black triangles with error bars in Fig. 6, respectively).

Thus we have a set of realistic PDFs, denoted by subscript i, and four potential I_{CO}–A_V relations, which we denote with the subscript j. We calculate a plausible set of CO intensities emergent from each cloud plus relation (i, j) for each of a range of metallicities, Z:

$$\text{PDF}\left(I_{\text{CO},i,j}(Z)\right) = f_j^{\text{CO},A_V}(A_{V,i}(Z)), \tag{8}$$

where $\text{PDF}(I_{\text{CO},i,j}(Z))$ is a PDF of CO intensity at metallicity Z for A_V PDF i and assumed I_{CO}–A_V relation j.

To estimate X_{CO}, we need to compare the emergent CO intensity to the amount of molecular hydrogen gas, $\Sigma_{\text{H}_2,i}(Z)$. This requires one additional step, which is to differentiate between H_2 and $H\,\textsc{i}$ in the PDF. Krumholz, McKee & Tumlinson (2009) and McKee & Krumholz (2010) argue that the layer of $H\,\textsc{i}$ in a molecular cloud can be described as a shielding layer of nearly fixed extinction and observations of Perseus support this (Lee et al. 2012; see also Wolfire et al. 2010; Sternberg et al. 2014). In detail, however, the depth of this layer may vary with metallicity, the radiation field, and volume density (e.g. see Wolfire et al. 2010). Here we will adopt a simple approach and adopt a constant $A_V^{\text{H}\,\textsc{i}} \sim 0.2$ mag for each cloud. We take all gas with A_V below this value to arise purely from atomic gas and so do not book-keep it when summing the PDF to

obtain an H_2 gas mass. A more realistic treatment of this H_2–$H\,\textsc{i}$ transition represents a logical extension of this calculation. Here we will only note when this becomes a dominant consideration.

In this approach

$$\text{PDF}\left(\Sigma_{\text{H}_2}\right) = \begin{cases} \text{PDF}(\Sigma_{\text{H}}) & \text{if } A_V > A_V^{\text{H}\,\textsc{i}}, \\ 0 & \text{if } A_V < A_V^{\text{H}\,\textsc{i}}, \end{cases} \tag{9}$$

where $A_V^{\text{H}\,\textsc{i}}$ is the extinction depth of the $H\,\textsc{i}$ shielding layer around the cloud.

Combining these equations, we generate I_{CO} and H_2 distributions as a function of metallicity, cloud structure, and I_{CO}–A_V mapping. Then, the CO-to-H_2 conversion factor is simply the total amount of H_2 column density divided by the total amount of I_{CO}:

$$\frac{X_{\text{CO},i,j}(Z)}{X_{\text{CO},i,j}(\text{Z}_\odot)} = \frac{\int \text{PDF}\left(\Sigma_{\text{H}_2,i}(Z)\right)}{\int \text{PDF}\left(I_{\text{CO},i,j}(Z)\right)} \frac{\int \text{PDF}\left(I_{\text{CO},i,j}(\text{Z}_\odot)\right)}{\int \text{PDF}\left(\Sigma_{\text{H}_2,i}(\text{Z}_\odot)\right)}. \tag{10}$$

By calculating X_{CO} relative to the solar metallicity value, the solar metallicity DGR drops out.

Fig. 9 shows the result of the procedure illustrated in Fig. 8, X_{CO} as a function of metallicity (dust-to-gas ratio). In Fig. 9, each panel shows the result for the different adopted I_{CO}–A_V relation. In each panel, different curves indicate different A_V PDFs drawn from Kainulainen et al. (2009). Grey lines indicate power law dependences of X_{CO} on metallicity for comparison.

This figure illustrates a few points. First, for most adopted PDFs and scalings, between about solar metallicity and $\sim 1/3\,Z_\odot$ we expect $X_{\text{CO}} \propto Z^{-1}$–$Z^{-2}$, i.e. we expect a moderately non-linear scaling in this regime. This is consistent with a number of theoretical and empirical results summarized in Bolatto et al. (2013), including results from dust (Israel 1997; Leroy et al. 2011) and star formation scaling arguments (Genzel et al. 2012; Schruba et al. 2012; Blanc et al. 2013). It is steeper than most virial mass-based results (Wilson 1995; Rosolowsky et al. 2003; Leroy et al. 2006; Bolatto et al. 2008). The constraint here can be phrased as follows: if local cloud PDFs are rescaled lower dust-to-gas ratios with no other change in the cloud physics, we might expect X_{CO} on the scale of whole clouds to scale as Z^{-1} to Z^{-2}.

Second, the calculation becomes very sensitive to the H_2–$H\,\textsc{i}$ prescription, the shape of the PDF, and the adopted I_{CO}–A_V relation at low metallicity. Even as high as $1/3\,Z_\odot$ these factors create a substantial (factor of 2) spread among our results. Below this value they dominate the results. At some level the spread in our estimates corresponds to a spread in nature, so that this highlights intrinsic scatter or uncertainty in the use of CO to trace H_2 at low metallicities. In this regime, large parts of a cloud may be $H\,\textsc{i}$, any threshold for CO emission will become incredibly important, and any power-law tail or extension to high A_V will be preferentially very good at emitting CO. This simple PDF-based approach argues for intrinsic uncertainties of order a factor of a few when using CO to trace H_2 below about $1/3$ solar metallicity.

Finally, though not our focus, the extension of these trends to supersolar metallicity suggests that a factor of ~ 2 change in X_{CO} could be achieved by bringing the solar neighbourhood clouds to even higher metallicity (and so stronger shielding). At the same time one might expect a number of other changes in the ISM, such as the emergence of a widespread diffuse molecular phase. But put simply, if all of the molecular gas in the Milky Way were better shielded, as one might expect for identical clouds dropped into a more dust-rich system, the conversion factor might be expected to be a factor of ~ 2 lower (Planck Collaboration XIX 2011). This is not clearly observed (e.g. Donovan Meyer et al. 2013; Sandstrom et al. 2013), but is also not clearly ruled out by observations given
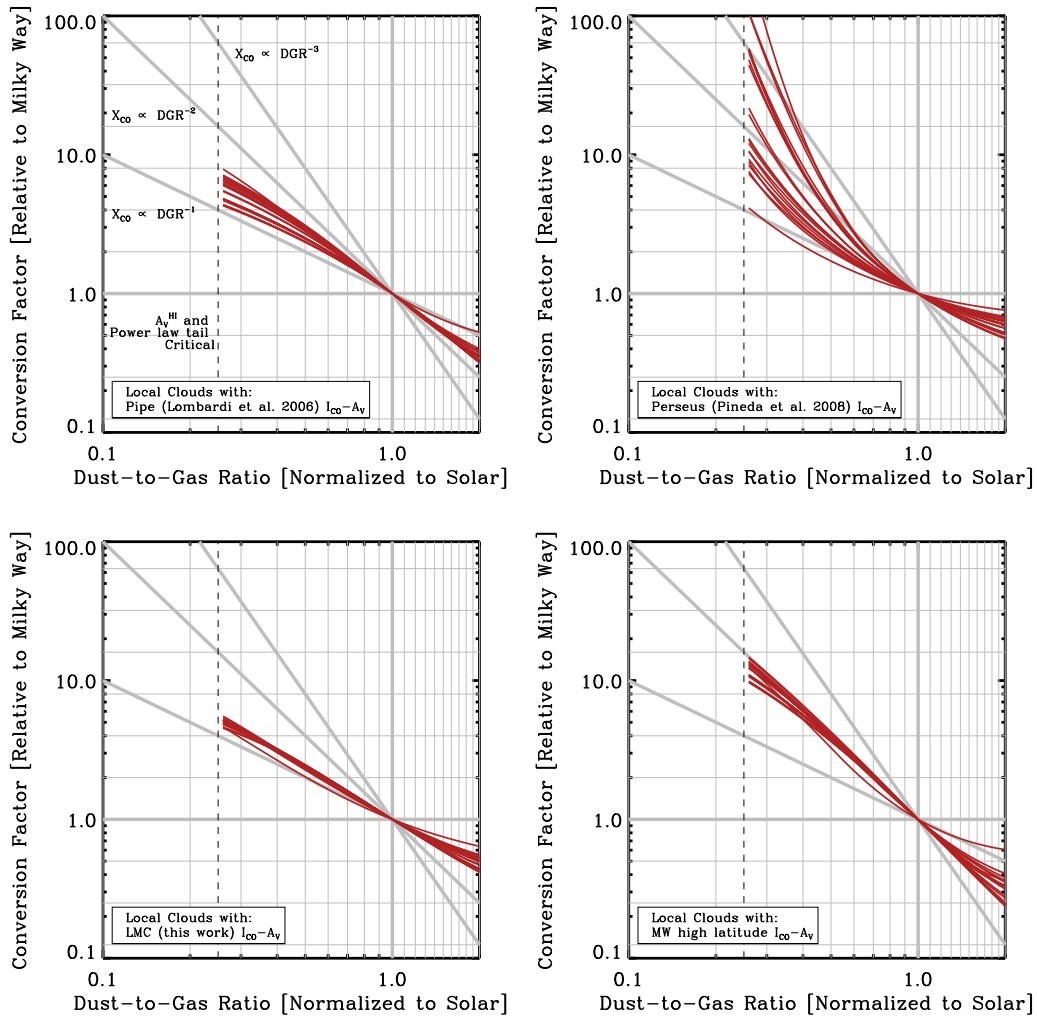
Figure 9. X_{CO} as a function of dust-to-gas ratio (and thus metallicity), estimated from the A_V PDF observed for Milky Way clouds (Kainulainen et al. 2009) and various I_{CO}–A_V relations [Pipe (left top): Lombardi et al. 2006; Perseus (right top): Pineda et al. 2008; LMC (left bottom), Milky Way high latitude (right bottom): polynomial fits to their average I_{CO}–A_V relations]. We compute X_{CO} as a function of dust-to-gas ratio following the illustration in Fig. 8 (see text for details). Each panel shows results for a different functional form of $I_{CO}(A_V)$, while the different red curves in each panel represent the different PDFs from Kainulainen et al. (2009). The dashed vertical line denotes a dust-to-gas ratio below which the assumed A_V threshold for the H I envelope (A_V^{HI}) and the power-law tail in the A_V PDF become critical in the calculation of CO emission. Thick light grey lines indicate X_{CO} as a function of dust-to-gas ratio with different power-law slopes ($X_{CO} \propto DGR^{-\alpha}$ with $\alpha = 1$, 2, and 3). Just below solar metallicity, X_{CO} is inversely correlated with metallicity with tractable scatter (α is between 1 and 2). However, by $\sim 1/3$ solar metallicity the input PDF, $I_{CO}(A_V)$, and assumed H I layer dominate the calculation that X_{CO} scatters by two orders of magnitude. Fundamentally this reflects the instability of using only a very small fraction of the cloud area to trace its total mass and the calculation undermines the utility of CO to study analogues of local clouds at even moderately subsolar metallicities. (A colour version of this figure is available in the online journal.)

that the link between Milky Way and extragalactic observations remains uncertain at the 10s of per cent level.

4.2 Physics, key unknowns, and complicating factors in the I_{CO}–A_V relation

In calculating X_{CO}, the Perseus I_{CO}–A_V stands out because it includes a hard A_V threshold for CO emission. This is particularly stark in Fig. 8 as below about 1/3 solar metallicity almost none of the PDF exceeds the Perseus threshold, suggesting an almost totally CO-dark cloud. Such a threshold is not visible in our Magellanic Cloud measurements, nor is the saturation in CO intensities found at high A_V in both the Pipe and Perseus. This is more likely a reflection of our coarse resolution than the absence of these physical features in the Magellanic Clouds.

In the appendix, we demonstrate the presence of substantial beam dilution in stacked LMC spectra by comparing line widths – which stay about constant – and peak temperatures – which drop to unphysical low levels at low A_V. This means that we read our observations results as consistent with a universal subresolution I_{CO}–A_V relation, but not as proof of such a relation. Future measurements comparing dust column density to CO emission across diverse environments will be needed to establish this relation and its variation at high (~ 0.1 pc, matched to molecular cloud substructure) resolution. Doing so, key questions will be the following.

(i) What is the form of the I_{CO}–A_V relation at low extinction? Is there a threshold or steepening of the relation at ≈ 0.5 mag? Does this also appear in highly resolved maps of the Magellanic Clouds?

(ii) How does the I_{CO}–A_V change with ambient radiation field? In a first study of this sort, Indebetouw et al. (2013) found evidence for suppressed CO emission at low A_V in regions illuminated by the strong radiation field of 30 Doradus.

(iii) Is the saturated regime important on the scale of integrals over whole clouds?

(iv) What is the intrinsic scatter in I_{CO} as a given A_V? This captures the degree to which this one-dimensional approach represents a reasonable shorthand for the complex geometry of real clouds.

A useful goal to enable the sort of calculation we describe above would be a library of relations that capture the realistic spread among this relation in the Milky Way and Magellanic clouds and allows for an understanding of how the key features such as the threshold, scatter at fixed A_V, saturation level, and dependence on environment.

Our knowledge of the PDF requires similar refinement. The PDF of Milky Way clouds at low column remains substantially unknown (Lombardi, Alves & Lada 2015), leading to uncertainties in the functional form of the gas distribution. Similarly, direct knowledge of the PDF of clouds in other galaxies is almost totally lacking. In the coming years both advances will help our understanding of the physics of CO emission substantially.

Finally, a careful handling of the different phases of the ISM will improve our understanding of the situation. We have adopted a very direct observational approach in this paper, simply considering all dust and CO in each ≈10 pc Magellanic Cloud beam. Via comparison with H I it should eventually be possible to model line of sight contamination by dust unassociated with the cloud, though this introduces subtleties regarding what dust is relevant for shielding. An improved analytic treatment of the H I–H$_2$ breakdown could also help refine the calculation.

5 SUMMARY

We show that at 10 pc resolution the relationship between dust column expressed as visual extinction and CO intensity appears similar in the low-metallicity Magellanic Clouds and the Milky Way. This agreement across a range of metallicity supports the theoretically motivated view of shielding by dust as the dominant factor in determining the distribution of bright CO emission. To show this, we use surveys of CO emission from the LMC (Wong et al. 2011) and SMC (Rubio et al., in preparation). We combine these with estimates of A_V based on *Herschel* IR maps from the HERITAGE survey (Meixner et al. 2010). We compare the Magellanic Cloud measurements to highly resolved Milky Way observations for two clouds, matched resolution measurements for local molecular clouds, and high-latitude CO and dust emission as seen by *Planck*.

Our measurements are consistent with an approximately universal relationship between CO intensity and dust extinction within molecular clouds, though with only ≈10 pc resolution we do not conclusively demonstrate such a relationship. Even for an approximately universal relation, we still expect such a relationship to vary at second order due to changing geometry and environment. We show suggestive evidence for such a variation in the LMC, where lines of sight with cooler dust temperatures show brighter CO emission at fixed A_V. This could indicate that the weaker radiation field in these regions lowers the density of dissociating photons, allowing CO to emerge at fainter A_V.

We discuss the implications of a nearly universal I_{CO}–A_V relationship and suggest a simple, separable model for thinking about integrated CO emission from molecular clouds. In this picture, the PDF of column densities, the dust-to-gas ratio, the I_{CO}–A_V relation, and the H$_2$–H I boundary combine to determine the properties of a cloud but can be treated as separate problems. A number of studies have already considered parts of this problem as separable. Here we explore the implications for the CO-to-H$_2$ conversion factor of a varying dust-to-gas ratio and fixed I_{CO}–A_V relation. Taking the PDF of local molecular clouds, we calculate the corresponding A_V distribution for a range of dust-to-gas ratios and then predict the CO emission for each case. The result is a prediction for the variation of CO-to-H$_2$ conversion factor.

Our empirically motivated model predicts $X_{CO} \propto Z^{-1}$ to Z^{-2} in above about $1/3\,Z_\odot$, in rough agreement with a variety of previous observational and theoretical studies. Our calculation also highlights the tenuous nature of CO as a tracer of molecular mass at metallicities even as high as $1/5\,Z_\odot$. At these metallicities, both the details of the H$_2$–H I transition and the shape of the high end of the column density PDF will be extremely important to X_{CO}. For a range of reasonable assumptions our calculations yield X_{CO} that can scatter by as much as an order of magnitude at these metallicities. Future work will be useful to establish the functional form and variation of the I_{CO}–A_V relation and PDF within clouds, including those at low metallicity and in other Local Group galaxies.

REFERENCES

Aguirre J. E. et al., 2003, ApJ, 596, 273
Aniano G., Draine B. T., Gordon K. D., Sandstrom K., 2011, PASP, 123, 1218
Bell T. A., Roueff E., Viti S., Williams D. A., 2006, MNRAS, 371, 1865
Bernard J.-P. et al., 2008, AJ, 136, 919
Blanc G. A. et al., 2013, ApJ, 764, 117
Bohlin R. C., Savage B. D., Drake J. F., 1978, ApJ, 224, 132
Bolatto A. D., Leroy A., Israel F. P., Jackson J. M., 2003, ApJ, 595, 167
Bolatto A. D., Leroy A. K., Rosolowsky E., Walter F., Blitz L., 2008, ApJ, 686, 948
Bolatto A. D., Wolfire M., Leroy A. K., 2013, ARA&A, 51, 207
Boulanger F., Abergel A., Bernard J.-P., Burton W. B., Desert F.-X., Hartmann D., Lagache G., Puget J.-L., 1996, A&A, 312, 256
Dame T. M., Hartmann D., Thaddeus P., 2001, ApJ, 547, 792
Dobashi K., Bernard J.-P., Hughes A., Paradis D., Reach W. T., Kawamura A., 2008, A&A, 484, 205
Donovan Meyer J. et al., 2013, ApJ, 772, 107
Downes D., Solomon P. M., 1998, ApJ, 507, 615
Draine B. T., Lee H. M., 1984, ApJ, 285, 89
Draine B. T. et al., 2007, ApJ, 663, 866
Dupac X. et al., 2003, A&A, 404, L11
Fukui Y. et al., 1999, PASJ, 51, 745
Fukui Y. et al., 2008, ApJS, 178, 56
Garay G., Johansson L. E. B., Nyman L.-Å., Booth R. S., Israel F. P., Kutner M. L., Lequeux J., Rubio M., 2002, A&A, 389, 977
Genzel R. et al., 2012, ApJ, 746, 69
Glover S. C. O., Mac Low M.-M., 2011, MNRAS, 412, 337
Gordon K. D. et al., 2010, A&A, 518, L89

Heiderman A., Evans N. J., II, Allen L. E., Huard T., Heyer M., 2010, ApJ, 723, 1019

Hildebrand R. H., 1983, QJRAS, 24, 267

Hughes A. et al., 2010, MNRAS, 406, 2065

Indebetouw R. et al., 2013, ApJ, 774, 73

Israel F. P., 1997, A&A, 328, 471

Kainulainen J., Beuther H., Henning T., Plume R., 2009, A&A, 508, L35

Kalberla P. M. W., 2003, ApJ, 588, 805

Keller S. C., Wood P. R., 2006, ApJ, 642, 834

Kennicutt R. C., Evans N. J., 2012, ARA&A, 50, 531

Kim S., Staveley-Smith L., Dopita M. A., Sault R. J., Freeman K. C., Lee Y., Chu Y.-H., 2003, ApJS, 148, 473

Krumholz M. R., McKee C. F., Tumlinson J., 2009, ApJ, 693, 216

Kutner M. L. et al., 1997, A&AS, 122, 255

Lee M.-Y. et al., 2012, ApJ, 748, 75

Lequeux J., Le Bourlot J., Pineau des Forets G., Roueff E., Boulanger F., Rubio M., 1994, A&A, 292, 371

Leroy A., Bolatto A., Walter F., Blitz L., 2006, ApJ, 643, 825

Leroy A., Bolatto A., Stanimirovic S., Mizuno N., Israel F., Bot C., 2007, ApJ, 658, 1027

Leroy A. K. et al., 2009, ApJ, 702, 352

Leroy A. K. et al., 2011, ApJ, 737, 12

Lombardi M., Alves J., Lada C. J., 2006, A&A, 454, 781

Lombardi M., Alves J., Lada C. J., 2015, A&A, 576, L1

McKee C. F., Krumholz M. R., 2010, ApJ, 709, 308

Maloney P., Black J. H., 1988, ApJ, 325, 389

Meixner M. et al., 2006, AJ, 132, 2268

Meixner M. et al., 2010, A&A, 518, L71

Meixner M. et al., 2013, AJ, 146, 62

Narayanan D., Krumholz M. R., Ostriker E. C., Hernquist L., 2012, MNRAS, 421, 3127

Pineda J. E., Caselli P., Goodman A. A., 2008, ApJ, 679, 481

Pineda J. L., Ott J., Klein U., Wong T., Muller E., Hughes A., 2009, ApJ, 703, 736

Pineda J. L., Goldsmith P. F., Chapman N., Snell R. L., Li D., Cambrésy L., Brunt C., 2010, ApJ, 721, 686

Planck Collaboration XVII, 2011, A&A, 536, A17

Planck Collaboration XIX, 2011, A&A, 536, A19

Planck Collaboration XXV, 2011, A&A, 536, A25

Planck Collaboration XI, 2014, A&A, 571, A11

Planck Collaboration XIII, 2014, A&A, 571, A13

Rémy-Ruyer A. et al., 2014, A&A, 563, A31

Rosolowsky E., Engargiola G., Plambeck R., Blitz L., 2003, ApJ, 599, 258

Rubio M., Lequeux J., Boulanger F., 1993, A&A, 271, 9

Sandstrom K. M. et al., 2013, ApJ, 777, 5

Schlegel D. J., Finkbeiner D. P., Davis M., 1998, ApJ, 500, 525

Schnee S. L., Ridge N. A., Goodman A. A., Li J. G., 2005, ApJ, 634, 442

Schnee S., Bethell T., Goodman A., 2006, ApJ, 640, L47

Schnee S., Kauffmann J., Goodman A., Bertoldi F., 2007, ApJ, 657, 838

Schnee S., Li J., Goodman A. A., Sargent A. I., 2008, ApJ, 684, 1228

Schruba A. et al., 2011, AJ, 142, 37

Schruba A. et al., 2012, AJ, 143, 138

Shetty R., Glover S. C., Dullemond C. P., Klessen R. S., 2011, MNRAS, 412, 1686

Skibba R. A. et al., 2012, ApJ, 761, 42

Stanimirovic S., Staveley-Smith L., van der Hulst J. M., Bontekoe T. R., Kester D. J. M., Jones P. A., 2000, MNRAS, 315, 791

Sternberg A., Le Petit F., Roueff E., Le Bourlot J., 2014, ApJ, 790, 10

van Dishoeck E. F., Black J. H., 1988, ApJ, 334, 771

Welty D. E., Xue R., Wong T., 2012, ApJ, 745, 173

Westerlund B. E., 1997, The Magellanic Clouds. Cambridge Univ. Press, Cambridge

Wilson C. D., 1995, ApJ, 448, L97

Wolfire M. G., Hollenbach D., McKee C. F., 2010, ApJ, 716, 1191

Wong T. et al., 2011, ApJS, 197, 16

Zaritsky D., Harris J., Thompson I. B., Grebel E. K., 2004, AJ, 128, 1606

APPENDIX A: EFFECT OF BASELINE SUBTRACTION, A THICK GALACTIC H I DISC, AND 30-DORADUS ON THE I_{CO}–A_V RELATIONS

A1 Baseline subtraction

In MAGMA DR2, a single linear baseline with magnitude of order a few mK has been subtracted from all spectra. In this paper, we carry out an additional zeroth-order baseline subtraction from the MAGMA data cube pixel-by-pixel. Our local baseline has mean magnitude ≈ 1.2 mK with 39 mK rms scatter from position to position. Because we integrate the data cube over the whole velocity axis (266 channels with a channel width of ~ 0.5 km s^{-1}), this baseline will change the local integrated CO intensity by $\approx 0.2 \pm 5$ K km s^{-1}. In the left-hand panel of Fig. A1, we show the affect of our additional
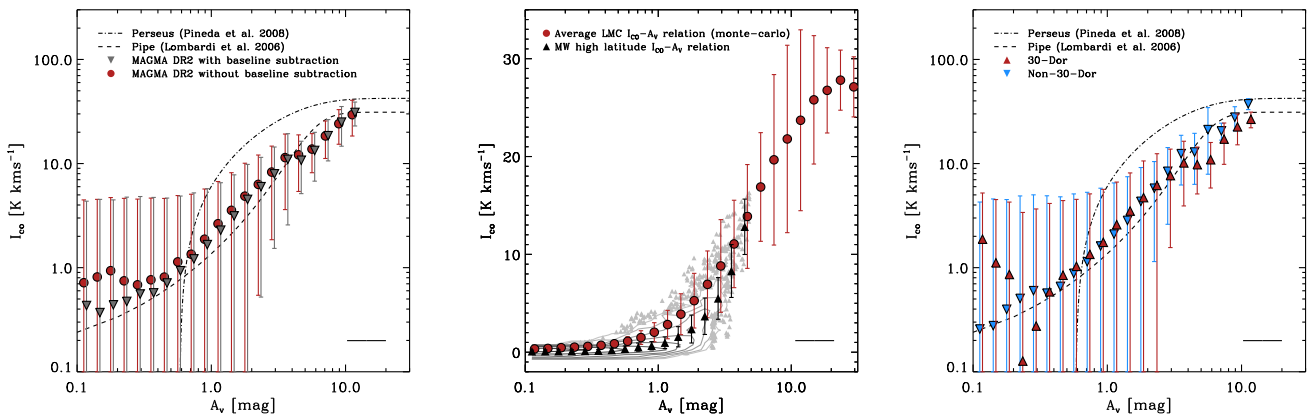

Figure A1. Left: effect of baseline subtraction, before (red circles) and after (grey downward triangles; shifted slightly towards right in *x*-axis for easier comparison) our correction. Additional baseline subtraction effectively removes the fixed level of CO emission at low A_V while leaving the relation unaffected at high A_V. Middle: I_{CO}–A_V relation in the high-latitude Milky Way lines of sight after subtracting the contribution of 400 pc thick H I disc to A_V (black triangles). The median I_{CO} at a given A_V in the high-latitude Milky Way lines of sight is now closer to the average LMC value (red circles), compared to Fig. 6. Right: I_{CO}–A_V relation in the LMC near 30 Doradus (red upward triangles) and outside 30 Doradus (blue downward triangles). Although there are differences at low A_V, there is no obvious strong effect associated with being near 30 Doradus above our completeness limit at $A_V \approx 0.8$ mag. (A colour version of this figure is available in the online journal.)

baseline subtraction on the I_{CO}–A_V relation in the LMC. The additional baseline correction effectively removes the CO emission at low A_V, which we thus interpret as likely artefacts. Overall, though, the relation does not change much and the baseline correction is almost irrelevant at high A_V.

A2 The contribution of the Milky Way's thick H I disc to A_V at high galactic latitudes

We argued that the I_{CO}/A_V for the high-latitude Milky Way is likely biased low because of contamination by dust associated with a long path length through the Milky Way H I disc. To estimate the magnitude of this effect, we compute a simple correction factor by adopting a typical hydrogen nuclei number density $n \approx 0.1\,\mathrm{cm^{-3}}$ for the warm neutral medium (WNM) component with a scale height of 400 pc at the location of the Sun (table 1 in Kalberla 2003). Assuming a typical Galactic dust-to-gas ratio, the A_V from this component would be

$$A_V = 0.1\,\mathrm{cm^{-3}} \frac{400\,\mathrm{pc} \times 3.09 \times 10^{18}\,\mathrm{cm\,pc^{-1}}}{\sin(b) \times 1.87 \times 10^{21}\,\mathrm{cm^{-2}\,mag^{-1}}}, \tag{A1}$$

where we convert column density to A_V adopting a Galactic dust-to-gas ratio ($N(\mathrm{H}) = 5.8 \times 10^{21} E(B - V)$; Bohlin et al. 1978) and $R_V = 3.1$, as in Section 3.4.

In the middle panel of Fig. A1, we show I_{CO}–A_V relation in the high Galactic latitude lines of sight in the Milky Way after correcting for the 400 pc thick Milky Way H I disc contribution to A_V. Compared to Fig. 6, the average trend of Milky Way high-latitude lines of sight in Fig. A1 is much closer to the average LMC I_{CO}–A_V relation.

A3 30-Dor versus non-30-Dor I_{CO}–A_V relations

In Section 3.3 we used the strength of ISRF traced by T_{dust} as a second parameter to test its effect on I_{CO}–A_V relation in the LMC. We also considered dividing the LMC into two regions, 30-Dor and Non-30-Dor (where 30-Dor region is defined as a rectangular box surrounding the H II region), to see if there is any systematic effect of star bursting environment on the I_{CO}–A_V relation. The I_{CO}–A_V relations in 30-Dor and non-30-Dor are shown in the right-hand panel of Fig. A1. Unlike the case for T_{dust}, we do not see any notable differences between the I_{CO}–A_V relations in 30-Dor and non-30-Dor, except at very low A_V lines of sight. We suspect that the weird behaviour of the relation at low A_V for 30-Dor region is likely arising from unstable baseline corrections towards CO faint lines of sight. Considering the large dispersion of I_{CO} at a given A_V, we conclude that there is no noticeable difference in the I_{CO}–A_V relation between the two regions.

APPENDIX B: STACKED SPECTRA FOR THE LMC

Our working assumption in the main text of the paper is that similar physics operate at small scales in molecular clouds in the LMC,

SMC, and Milky Way. We interpret the coincidence of LMC, SMC, and Milky Way data at low resolution in I_{CO}–A_V space to support this. A consequence of this conclusion is that the very low line-integrated intensities seen in the Magellanic Clouds are often a result of dilution by our 10-pc beam.

As a basic test of this, we stack the MAGMA spectra in bins of A_V and examine their peak temperature and line width in each bin. If beam dilution is the dominant physics in setting the observed stacked intensity, then we expect the peak temperature of the spectrum to vary monotonically with A_V and integrated intensity while the line width shows no clear trend. In this case the diminishing intensity simply represents averaging similar spectra with more and more empty space within the beam. We show that this is the case in Fig. B1, which plots CO spectra from LMC in bins of A_V. Before averaging, the velocity axis of the CO line has been shuffled using H I emission (Kim et al. 2003) as a template (following Schruba et al. 2011).

In Fig. B1, we show the stacked spectrum in each A_V bin as grey filled histograms. We fit a single Gaussian to each stacked spectrum to derive the peak brightness temperature (T_{pk}) and full width at half-maximum (FWHM) of the CO line. We overplot residuals from the Gaussian fit as red diagonally hatched histograms. Fig. B1 clearly shows that the peak brightness temperature increases as a function of A_V except in the last A_V bin where a mismatch of CO and H I velocity is apparent and leads to lower T_{pk} than the real value. On the other hand, the fit line width does not have a clear trend. It increases at low A_V and decreases at high A_V. Therefore, it appears that the peak main beam temperature drives the rise of integrated CO intensity as a function of A_V in the LMC.

The peak values lie far below the expected kinetic temperatures of the molecular gas, so we expect that the dominant factor in Fig. B1 is a changing level of beam dilution. Changing excitation may play some role as well; Pineda et al. (2008) found that the CO excitation temperature increases as a function of visual extinction in the Perseus molecular cloud (see fig. 10 of their paper), ranging from 5 K at low A_V to 20 K at high A_V. Increased heating associated with molecular peaks might also play a role, either due to enhanced star formation activity (e.g. Heiderman et al. 2010) or due to efficient photoelectric heating (Hughes et al. 2010).

Large beam dilution effects have been seen in the Magellanic Clouds as early as Rubio, Lequeux & Boulanger (1993) and Lequeux et al. (1994), when it was invoked to explain the weak CO emission in the SMC. It has also been noted in CO observations of the LMC using SEST telescope (Kutner et al. 1997; Garay et al. 2002). We show that this effect remains strong even at 10 pc resolution. The direct result of this calculation is that the I_{CO}–A_V relation in the Magellanic Clouds must be carefully interpreted. It will not straightforwardly encode features like saturation and an A_V threshold (see also Wong et al. 2011). However, once data are matched in scale, we expect that its similarity to Milky Way results does indicate similar physics operating at subresolution.
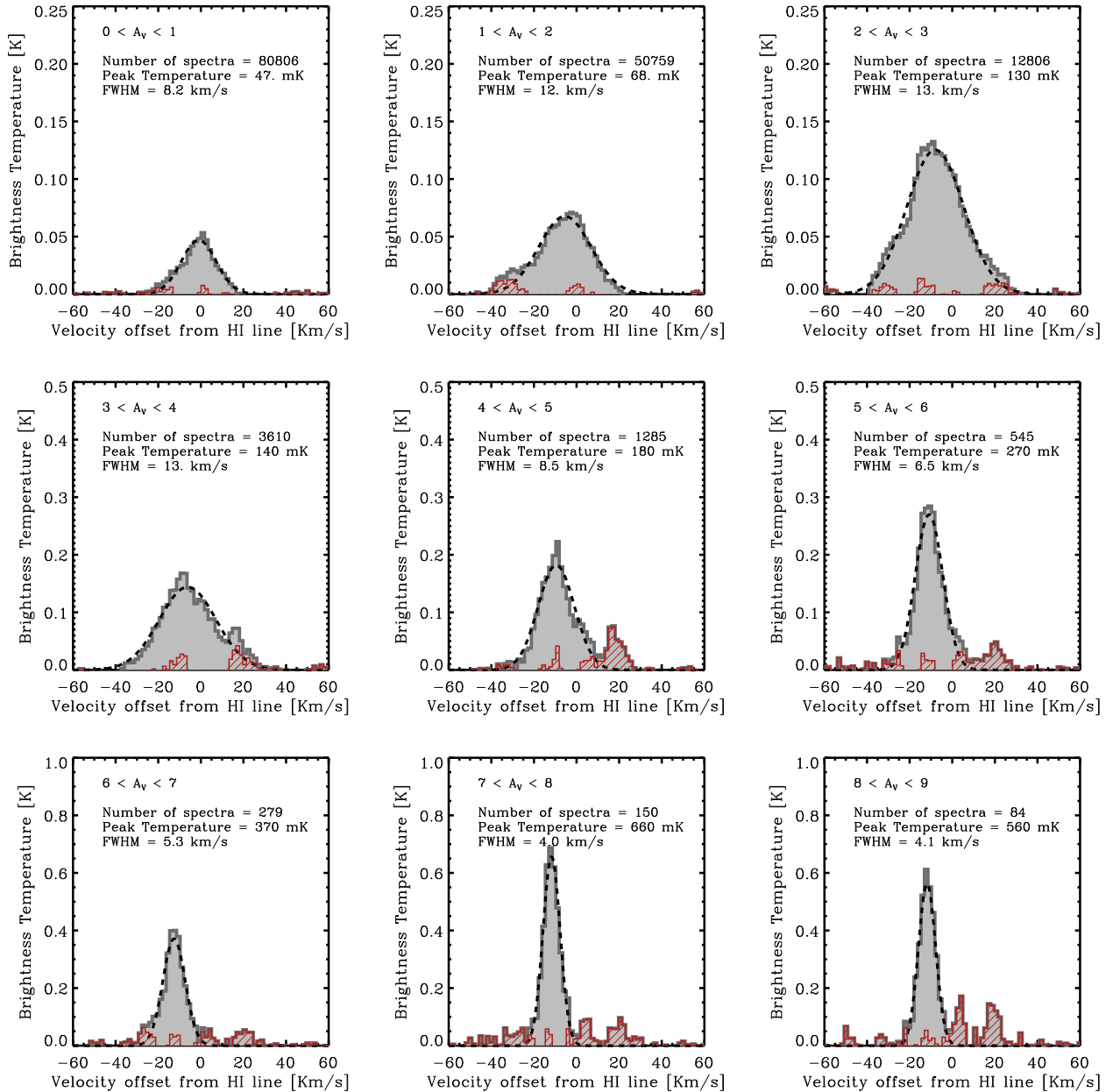
Figure B1. Stacked CO spectra in bins of A_V in the MAGMA field. Before stacking, we shuffled each spectrum using H I velocity field from Kim et al. (2003) data cube as a template, and fit a single Gaussian to shuffled spectra to estimate the peak brightness temperature (T_{pk}) and FWHM of the CO line. In each panel, grey filled histogram shows stacked spectra, smoothed slightly in velocity axis, and black dashed line shows Gaussian fit to the data. Best-fitting parameters are shown on the left top of each panel, and red diagonally hatched histogram shows the residuals from the fit. Significant offset between H I and CO velocities of order ~20 km s^{-1} can be identified in the CO spectra of high A_V bins, probably due to the fact that H I lines are often found with multiple components while CO lines usually have single component. In general, we find that the peak brightness temperature increases as a function of A_V, while there is no clear trend in velocity dispersion. (A colour version of this figure is available in the online journal.)

This paper has been typeset from a T$_{\rm E}$X/L^{A}T$_{\rm E}$X file prepared by the author.